Helena Biljanić, Barbara Markulić, Tadeja Kosec, Marija Mirosavljević, Vladan Desnica, Domagoj Šatović, Damir Kralj, Katarina Marušić

Electrochemical assessment of crosslinked self-assembled monolayers of behenic acid for enhanced corrosion protection of bronze and patinated surfaces

Progress in Organic Coatings

Volume 211

2026,

109750,

ISSN 0300-9440

https://doi.org/10.1016/j.porgcoat.2025.109750

Progress in Organic Coatings 211 (2026) 109750

Electrochemical Assessment of Crosslinked Self-Assembled Monolayers of Behenic Acid for Enhanced Corrosion Protection of Bronze and Patinated Surfaces

Helena Biljanić[a], Barbara Markulić[b], Tadeja Kosec[c], Marija Mirosavljević[a], Vladan Desnica[d], Domagoj Šatović[d], Damir Kralj[a], Katarina Marušić[a,*]

[a] Ruđer Bošković Institute, Division of Materials Chemistry, Laboratory for Precipitation Processes, Bijenička cesta 54, 10 000 Zagreb, Croatia

[b] Faculty of Chemical Engineering and Technology University of Zagreb, Trg Marka Marulića 19, 10 000 Zagreb, Croatia

[c] Slovenian National Building and Civil Engineering Institute, The Department of Materials, Laboratory for Metals, Corrosion and Anti-Corrosion Protection, Dimčeva ulica 12, 1000 Ljubljana, Slovenia

[d] Academy of Fine Arts, University of Zagreb, Ilica 85, 10 000, Zagreb, Croatia

*corresponding author: kmarusic@irb.hr

Abstract

Bronze sculptures and historical artifacts typically develop natural or artificially induced patinas that enhance aesthetic value and confer some degree of corrosion protection. However, patinated surfaces are vulnerable to environmental degradation, especially due to acid rain, resulting in material loss and impaired visual integrity. Current protective coatings are limited by either environmental or performance constraints. While self-assembled monolayers (SAMs) based on fatty acids such as behenic acid offer potential corrosion protection by forming ultrathin layers on metal surfaces, their long-term effectiveness is compromised by limited chemical stability.

This study addresses this critical gap by evaluating the protective effectiveness and durability of SAMs and polymer nanocoatings (PNCs) derived by crosslinking SAMs from behenic acid using gamma irradiation on bare bronze (BB), black sulfide-patinated bronze (BP), and green chloride-patinated bronze (GP) surfaces. The assessment focused primarily on electrochemical performance, using electrochemical impedance spectroscopy (EIS) and potentiodynamic polarization (Tafel) measurements to evaluate coating stability and corrosion resistance before and after artificial ageing.

Initial surface characterization employed spectroscopic (FTIR-ATR, Raman spectroscopy), microscopic (SEM-EDS, metallography), elemental (X-ray fluorescence), wettability (contact angle goniometry), and visual analyses (colorimetry) to characterize the composition and morphology of the substrates. Distinct structural and chemical differences were identified, with BP characterized primarily by anilite (Cu_7S_4) and GP consisting predominantly of basic copper chlorides ($Cu_2(OH)_3Cl$), such as atacamite and its isomorphs.

Electrochemical analyses demonstrated that while SAM coatings initially reduced corrosion current densities significantly, their protective capability diminished over time due to progressive removal of loosely bound molecules. Conversely, radiation-crosslinked PNC coatings maintained stable corrosion protection over UV-Wet-Dry artificial ageing. Minor capacitance increases indicated slight enhancement in surface activity, yet no significant degradation of the crosslinked polymer coating was observed.

Keywords: bronze patina, self-assembled monolayer, radiation crosslinking, polymer nanocoating, corrosion protection

1. Introduction

Bronze has historically been among the most widely utilized materials for artistic and cultural heritage objects due to its favorable mechanical properties, workability, and appealing aesthetic qualities. Its use dates back millennia, notably for sculptures, monuments, and decorative artifacts, making the preservation of bronze surfaces both culturally significant and scientifically challenging. Bronze surfaces naturally develop patinas, thin corrosion layers formed primarily of copper-based compounds that impart aesthetic value while providing an initial protective barrier against environmental degradation.

Depending on environmental exposure, these patinas commonly include corrosion products such as cuprite (Cu_2O), brochantite ($Cu_4(OH)_6SO_4$), antlerite ($Cu_3(OH)_4SO_4$), and posnjakite ($Cu(OH)_6SO_4 \cdot H_2O$) in outdoor atmospheres, while malachite ($Cu_2(OH)_2CO_3$) and azurite ($Cu_3(OH)_2CO_3$) more typically form in burial environments [1]. In contrast, artificial patinas with controlled chemical compositions can be created through accelerated surface treatments [2], specifically tailored to achieve the desired color and appearance. These distinctions reflect differences in environmental chemistry and have critical implications for surface stability and conservation approaches. Recent comprehensive reviews provide detailed insights into the mechanisms and layered structures of both artistic and naturally developed patinas, highlighting their complexity and significance in cultural heritage contexts. Black patinas are typically produced using potassium sulfide, while green patinas result from treatments involving chlorides, nitrates, sulfates, or phosphates [3].

Despite the protective nature of patinas, their stability and durability under atmospheric conditions—particularly in urban environments—is severely compromised by acidic pollutants, notably acid rain. Acid rain accelerates patina dissolution, causing increased corrosion rates and progressive degradation that leads to irreversible aesthetic and structural damage. Moreover, frequent restoration interventions to remove corrosion products can exacerbate damage and material loss, necessitating the development of reliable long-term protective strategies. Protective coatings for cultural heritage must fulfill stringent requirements, including environmental friendliness, reversibility, transparency, durability, and minimal alteration of the artifact's aesthetic characteristics [4]. However, traditional protective systems often fall short, prompting research into alternative methods.

Protective treatments for patinas on bronze and other heritage metals commonly involve a combination of traditional and advanced coating systems to ensure long-term conservation and aesthetic preservation. Traditional waxes and acrylic resins such as Paraloid B-72 remain widely used due to their reversibility, transparency, and ease of application [5]. However, more durable and effective systems are increasingly employed, including fluoropolymer coatings and organosilane-based treatments, which offer superior water repellency, UV resistance, and adhesion to both the patina and metal substrate [5,6]. Recent studies have also demonstrated the effectiveness of combining corrosion inhibitors—particularly long-chain phosphonic acids—with acrylic coatings, significantly enhancing resistance to environmental degradation [6]. These multilayer systems provide a tailored protective strategy, balancing conservation ethics with performance requirements, especially for outdoor cultural heritage exposed to urban pollution and acid rain.

This study builds on previous research into corrosion-inhibiting coatings for bronze surfaces, including azole-based [2,7–16], organosilane-based [17–19], fluoropolymer-based [20–26], and phosphonic acid-based [23] coatings. Azole-based treatments, for instance, exhibit effective corrosion inhibition but may pose environmental concerns or limited longevity. Organosilane-based coatings offer good initial performance but often suffer deterioration under prolonged environmental exposure. Fluoropolymer-based systems provide considerable protection but can present reversibility issues and environmental concerns related to fluorinated compounds.

In contrast, self-assembled monolayers (SAMs), particularly those formed from organic molecules such as fatty acids or phosphonic acids, have recently attracted attention due to their ultrathin, uniform, and well-defined molecular organization, which is beneficial for preserving the visual integrity and texture of bronze surfaces. Fatty acid-based SAMs stand out as promising candidates due to their biodegradability, non-toxicity, and ability to form dense molecular films, even on irregular and rough surfaces characteristic of patinated bronze [27].

The adhesion of SAMs on metal substrates relies on chemisorption, where functional head groups interact with surface oxides and hydroxyl groups, forming stable, ordered layers. Factors such as substrate composition, reactive site density, and deposition conditions influence adhesion strength [28]. The presence of hydroxyl groups enhances interfacial bonding, improving stability and resistance to environmental degradation, while physical entrapment within the porous patina structure can provide additional adhesion support. A comprehensive understanding of both molecular interactions and macro-scale surface characteristics is crucial for optimizing coatings, ensuring durability, and enhancing long-term protection.

However, a significant limitation of SAM-based coatings is their relatively low chemical stability and mechanical durability, which reduces their effectiveness over prolonged exposure periods [29–32]. This limitation can potentially be overcome by transforming SAMs into crosslinked polymer nanocoatings (PNCs) [29,33–36]. Recent advances indicate that applying high-energy gamma radiation can effectively crosslink SAM layers into stable polymer matrices, significantly enhancing coating stability and durability. Radiation crosslinking induces radical polymerization reactions between the molecules of fatty acids initially organized into SAMs, creating molecularly thin yet robust polymer networks that resist chemical degradation and provide superior long-term corrosion protection compared to non-crosslinked SAMs. Nevertheless, while successful crosslinking of SAMs has been demonstrated on clean, flat metal surfaces, its applicability and efficacy on complex and irregular patinated bronze surfaces remain insufficiently explored, representing a critical research gap.

This study aims to systematically evaluate the corrosion-protective properties and long-term durability of behenic acid-based SAMs and radiation-crosslinked PNCs applied to bare bronze, black sulfide-patinated bronze, and green chloride-patinated bronze under simulated atmospheric conditions. It characterizes the structural, chemical, and electrochemical features of these bronze surfaces, assesses the comparative efficacy and durability of SAM coatings versus their gamma-irradiated PNC counterparts, and examines how variations in patina composition and structure affect coating adhesion, stability, and corrosion resistance.

2. Experimental

2.1. Sample preparation

The bronze used in this study is a commercial CuSn7ZnPb alloy (RG7, CC493K), supplied by Strojopromet d.o.o. (Croatia) and manufactured by BIKAR METALLE GmbH (Germany). While primarily classified as an industrial-grade material, lead-containing bronzes such as this are also commonly found in heritage objects, as evidenced by field analyses of public monuments and supported by literature [37]. Its conformity with specifications was verified through a factory certificate issued in accordance with EN 10204 - 3.1.

Table 1. Nominal chemical composition of the RG7 bronze.

	Cu	Pb	Sn	Zn	Fe	P	Ni	Al	S	Sb	Si
wt %	81-85	6-8	6.3-7.5	2-4	0.2	1.5	1.0	0.005	0.08	0.35	0.005

The bronze was delivered in the form of rods with a 1.3 cm diameter, in a cast and machined state, without any additional plastic deformation or heat treatment. The specimens were prepared by cutting slices from the rod 0.5 cm in thickness. Surface preparation was carried out using a Metkon Forcipol 102 polishing device with Galaxy diamond grinding discs (P180-320, P400-600 and P800-1000). Following abrasion, the samples were thoroughly washed under running tap water and degreased in ethanol using an ultrasonic bath for 10 min. Only one surface of each plate was subjected to subsequent treatments.

To reveal the microstructure, the bronze samples were chemically etched prior to SEM imaging using a 30 % $FeCl_3$ solution. A few drops of the etchant were applied directly to the polished surface and allowed to react for approximately 30 seconds. The etching process was then stopped by rinsing the samples with distilled water, followed by ethanol to remove residues and facilitate drying.

2.1.1. Preparation of patinas on bronze samples

Two patination methods commonly used in Southern Europe were examined. *Black patina (BP)* was produced by applying a 3 % potassium sulfide (K_2S) water solution to bronze. Bare bronze (BB) plates were preheated in an oven at 80 °C, and the solution was applied to the heated surface using a natural fiber brush in three successive layers. This process was repeated three times. To remove impurities, the BP samples were gently cleaned with a sponge and rinsed with redistilled water.

Green patina (GP) was prepared on top of BP using a water solution of ammonium carbonate $(NH_4)_2CO_3$ and ammonium chloride (NH_4Cl). Both salts were dissolved in water at concentrations of 3 g/dm^3. The obtained solution was further diluted in a 1:1 ratio with H_2O, to obtain the solution for creating GP. BP samples were heated in an oven for 30 minutes at 60 °C before the GP solution was applied in three layers, again using a natural fiber brush. After application, the samples were placed in a sealed petri dish along with a water-soaked cotton pad to maintain humidity for 24 hours [38].

While the bronze samples were polished to P1000 to ensure reproducibility and enable good comparison, the BP and GP samples developed patinas with inherently rough and porous surfaces. These are more representative of real historical bronzes. Nevertheless, this approach enabled us to isolate coating behavior on complex patinated substrates while maintaining reliable control samples.

2.1.2. Application of fatty acid to the surface (SAM preparation)

Behenic acid, $C_{21}H_{43}COOH$, a saturated fatty acid with 22 carbon atoms was purchased from Thermo Fisher Scientific, USA. Self-assembled molecular layers (SAMs) were prepared on BB, BP and GP samples. To create the SAM layer, the samples were immersed in a 1 mmol/dm^3 solution of behenic acid diluted in ethanol (96 %) at room temperature for 24 h.

Although dipping was used as the deposition method here due to its film uniformity, we previously demonstrated that SAM coatings can also be applied via brushing and spraying, showing promising results for real object applications [34].

2.1.3. Sample irradiation

Samples with a SAM on their surface were sealed in a glass flask and purged with argon to remove oxygen. Irradiation was performed at a panoramic gamma radiation facility using ^{60}Co at room temperature. The facility's dose distribution was mapped experimentally using an ionizing chamber and ethanol-chlorobenzene dosimeters, as well as through Monte Carlo simulation calculations [34,35]. Irradiation conditions were selected based on previous studies [29,34,36]. The absorbed dose applied for crosslinking was 110 kGy, administered at a dose rate of 11.8 kGy/h.

2.1.4. Artificial aging

The samples were artificially aged in a QUV accelerated weathering tester (Q-LAB, Germany). The chamber was equipped with UVB-313 lamps, according to a 10-day cycle-based protocol. Each cycle lasted 24 hours and consisted of three stages, all at a constant temperature of 50 °C, with no thermal cycling:

- UV irradiation for 4 hours, using a UVB-313 light source with irradiance set to 0.48 W/m^2/nm at 313 nm, simulating enhanced UV stress;
- Condensation phase for 4 hours at 100 % relative humidity (RH), simulating night-time dew or high-humidity conditions;
- Dry thermal exposure for 16 hours in a dry chamber environment, without additional moisture or radiation, to simulate extended warm and dry periods.

The total exposure time was 10 cycles (240 hours). This combination of UV, humidity, and dry phases aims to accelerate material degradation mechanisms in a controlled laboratory setting.

2.2. Characterization of the samples

Colorimetry. A Konica Minolta® CM-2600d spectrophotometer was used to measure the color of the samples. The measurements were taken over a 3 mm diameter area using diffuse illumination and 8° viewing, CIE Standard Illuminant D65 corresponding to the average daylight. Measurements were performed simultaneously by the Specular Component Included (SCI) and Specular Component Excluded (SCE) method. The spectrophotometer was configured to perform four consecutive measurements, with the results averaged to determine the color coordinates. To ensure precise color evaluation five measurements were performed on each sample.

Fourier transform infrared spectroscopy (FTIR). A PerkinElmer Spectrum Two spectrometer equipped with an attenuated total reflectance (ATR) module was used to identify functional groups present on the surface of the samples. FTIR spectra were collected at room temperature over a frequency range of 450-4000 cm^{-1}, with a resolution of 4 cm^{-1} and a total of four scans per measurement. The spectrum of each sample was recorded three times to ensure reproducibility and confirm a representative spectrum for each sample type. Following spectral collection, baseline correction was applied for accurate interpretation.

X-ray fluorescence (XRF). The samples were analyzed using a custom-made portable XRF instrument which features a 50-kV Rh transmission excitation tube (Moxtek, USA) and a Peltier-cooled silicon drift detector (Amptek, USA) with a 145 eV energy resolution at the Mn Kα line. The device offers both milli- and micro X-ray beams for sample excitation, using a motorized collimator system to switch between a 1.5 mm pinhole and a 65 µm polycapillary lens (IfG, Germany). Measurements were taken with a tube voltage of 40 keV, an anode current of 150 µA, and a 100 s acquisition time. For precise alignment, a two-laser system ensures the sample is correctly positioned in front of the X-ray source and detector. Two measurements were taken per sample, and the results were averaged.

Metallography. Metallographic sections were prepared by cold cut cross-sections of the specimens, hot-mounted in PolyFast bakelite resin with carbon filler and grinded using CarbiMet (320-grit SiC paper), TexMet C (9 µm), VerduTex (3 µm), VerduTex (1 µm) and ChemoMet (0.02-0.06 µm). Observations were conducted using a Zeiss Axio Imager Z2m microscope with Zen software (Carl Zeiss AG, Aalen, Germany), using bright field light.

Scanning electron microscopy (SEM) and energy-dispersive X-ray spectroscopy (EDS). Surface and cross-sectional characterization of the samples was performed using an Axia™ ChemiSEM™ SEM (Thermo Fisher Scientific, Waltham, MA, USA) equipped with an EDS system. Samples were mounted onto the specimen holder using conductive double-sided adhesive carbon tape. SEM and EDS analyses were carried out on both the surface and cross-section of the samples. For surface imaging, an Everhart-Thornley Detector (ETD) was used at a magnification of 5000×, an accelerating voltage of 10 kV, a working distance of 10.2 mm, and a horizontal field width of 25.4 µm. For cross-sectional imaging, the same detector and magnification were applied, but with an accelerating voltage of 15 kV, a working distance of 9.8 mm, and a horizontal field width of 25.4 µm.

Contact angle goniometry. The contact angles were measured using a DataPhysics contact angle system OCA 20 goniometer, employing the sessile drop method with a 2 µL drop of water under ambient atmospheric conditions. Six measurements were performed on each sample.

Electrochemical investigations. The protective properties of the coatings were evaluated using electrochemical methods in a three-electrode system. Samples were placed into corrosion cell holders designed for cylindrical specimens, with the exposed surface area of the working electrodes being 0.5 cm^2. A platinum foil was used as a counter electrode, and a saturated calomel electrode (SCE) was used as the reference electrode. All potential values reported in the text refer to the SCE scale.

The test solution, referred to in the text as the *corrosion test solution*, was an aqueous mixture containing 0.2 g/dm^3 each of $NaHCO_3$, Na_2SO_4, and $NaNO_3$, acidified to pH 5 using diluted H_2SO_4 to simulate atmospheric corrosion conditions. The measured conductivity of the solution was approximately 2.1 mS/cm at room temperature. This simplified formulation was chosen to provide a controlled, reproducible, and chemically relevant exposure environment for evaluating the performance of protective coatings. The selected salts represent key ionic species typically found in atmospheric deposition: bicarbonates (components derived from CO_2), sulfates (from SO_2 emissions), and nitrates (from NO_x emissions), which are major contributors to acid rain and surface degradation. Chlorides were excluded from the test solution, as the study focused on simulating urban atmospheric environments without marine influence. The pH value of 5 reflects the upper range of acid rain levels commonly reported in southern Europe over the past decade. Although more complex and site-specific artificial rain formulations have recently been proposed [39], this study prioritizes standardization and comparative assessment of coating behavior under broadly representative conditions. Before conducting electrochemical measurements, the electrodes were immersed in the corrosion test solution for 45 minutes to allow stabilization of the open circuit potential (OCP).

Firstly, electrochemical impedance spectroscopy (EIS) was carried out at OCP across a frequency range from 100 kHz to 10 mHz with an applied signal amplitude of 10 mV rms. After that, polarization measurements were performed in a wide (±150 mV OCP) potential range with a potential scan rate of 0.166 mV/s. All electrochemical measurements were performed at room temperature using a PalmSens4 potentiostat/galvanostat/impedance analyzer.

No iR (ohmic drop) compensation was applied during polarization testing; however, all samples were measured under identical conditions. As such, the reported corrosion current densities should be interpreted as comparative indicators of coating performance rather than absolute values.

The preparation procedure was consistently applied to five samples using the same method. The parameters presented in the manuscript represent the mean values.

Raman spectroscopy. The Raman spectra of the investigated patinas and coating systems were recorded using 632 nm laser excitation lines using a Horiba Jobin Yvon LabRAM HR800 Raman spectrometer (Horiba Yvon, France, 2008), coupled with an Olympus BXFM optical microscope (Olympus, UK, 2008). The spectra were recorded using a 100× objective lens and 600 grooves/mm grating, which gave a spectral resolution of cca. 1 cm^{-1} /pixel. A multi-channel, air-cooled CCD detector was used, with integration times of between 20 and 35 s, and the spectral range was set to between 80 and 1000 cm^{-1} for patinas and 80 to 4000 cm^{-1} for coatings. The spectra are presented with no baseline correction.

3. Results and Discussion

This study aims to investigate the protective properties of self-assembled monolayers (SAMs) and polymer nanocoatings (PNCs) based on behenic acid, crosslinked via ionizing radiation, in mitigating corrosion of bare bronze (BB) and patinated surfaces exposed to acid rain. Two preparation methods commonly used in Southern Europe for preparing patina were examined: a patina created through the application of potassium sulfide directly onto bronze (black patina, BP), and a patina formed over the BP using ammonium carbonate and ammonium chloride (green patina, GP).

3.1. Bare patinas

Colorimetric measurements were conducted on BB, BP and GP samples to provide an objective and quantifiable means of visually confirming the color of the formed patinas, with the results presented in Fig. 1. Notably, significant differences between SCI and SCE values were observed only for the BB samples, attributable to the gloss characteristic of bare metal, a feature absent in patinas. The a^* and b^* values for BB samples are predominantly positive, indicating red and yellow hues which combine to produce the characteristic orange color of BB, as illustrated in the corresponding photograph in Fig. 1. In contrast, BP samples exhibit *a** and *b** values close to zero, with *L** emerging as the primary distinguishing parameter. This indicates that BP lacks additional pigments and is uniformly black, as corroborated by its photograph in Fig. 1. GP samples exhibit a negative *a** value, reflecting a green hue, as evident in Fig. 1. Consistent with these observations, the patinas are referred to in the text as black patina (BP) and green patina (GP).

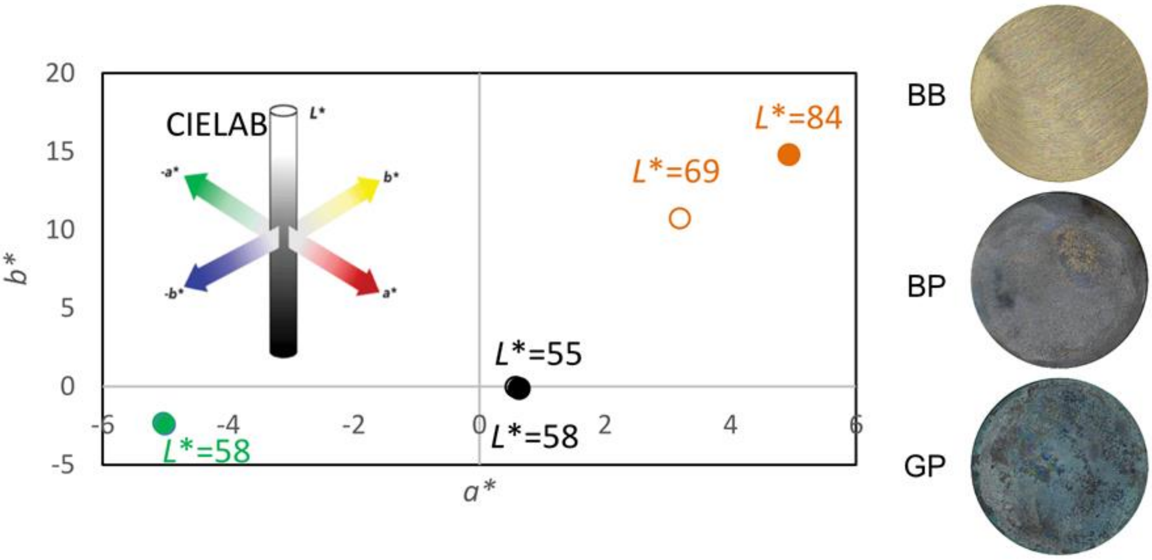

Figure 1. Colorimetric parameters for bare bronze (BB, orange), black patina (BP, black), green patina (GP, green) samples. Filled markers denote SCI values, while empty markers represent SCE values. Included are photographs of BB, BP and GP samples.

The SEM micrographs of etched BB, in addition to BP and GP samples are presented in Fig. 2. The etched BB sample (Fig. 2a) clearly reveals microstructural features characteristic of a leaded tin bronze alloy. The image clearly displays the typical multiphase microstructure of cast leaded bronze, including the α-Cu matrix, intermetallic δ-phase (Cu-Sn compounds), and Pb-rich inclusions. The BP sample (Fig. 2b) displays a bronze surface uniformly covered by patina, which is notably rougher that the smooth BB surface. The GP sample (Fig. 2c) exhibits a visibly more intricate structure compared to both BB and BP.

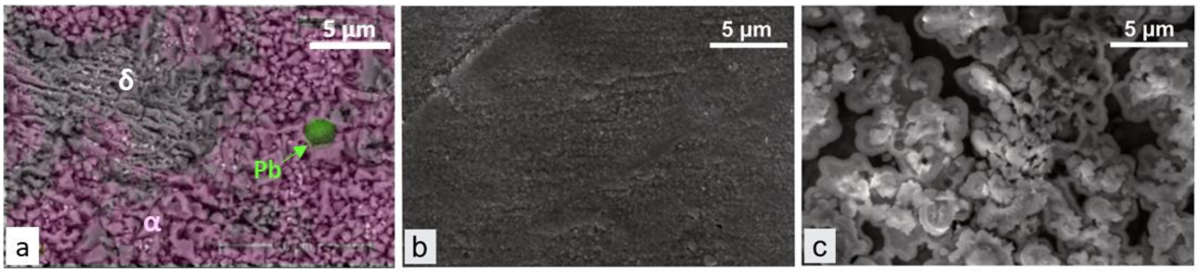

Figure 2. SEM micrographs of the surfaces of (a) etched BB, (b) BP, and (c) GP.

The XRF spectra obtained on the samples (Fig. 3) reveals presence of all elements characteristic of RG7 bronze, as presented in Table 1. In addition to these elements, the BP sample exhibits a distinct peak related to sulfur, while the GP exhibits a peak related to chloride. These observations indicate that the BP is sulfur-based and the GP is chloride-based, consistent with the chemical solutions used in their preparation. These findings are corroborated by EDS analysis presented in Table 2.

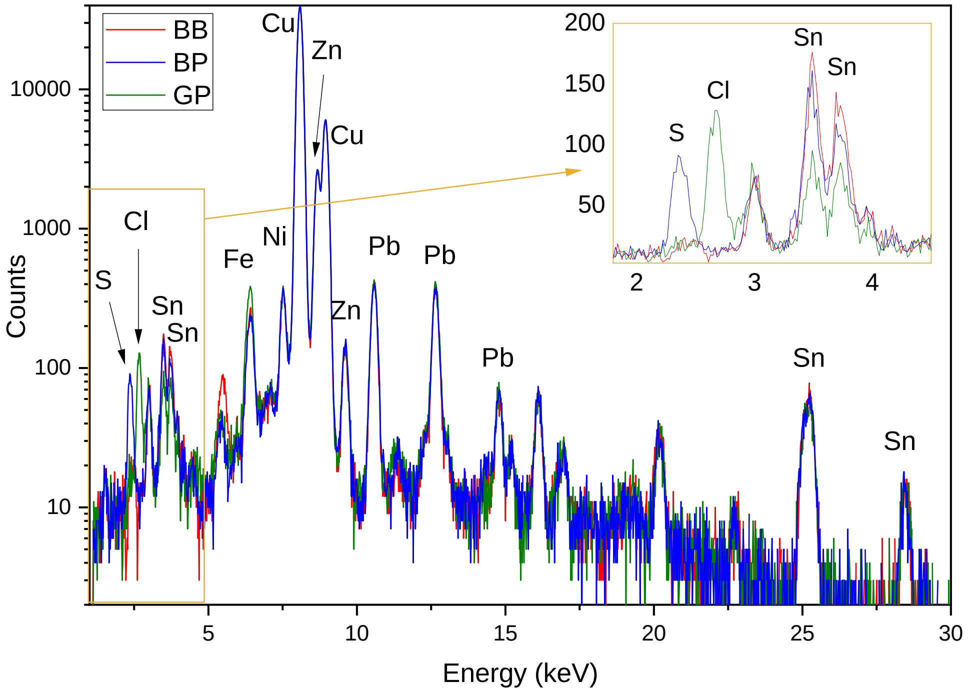

Figure 3. The XRF spectra of all three samples.

The composition of the bronze aligns with typical RG7 specifications, with copper, tin, zinc and lead as the most prominent elements. It is important to note that the elemental data in Table 2 were obtained via EDS, which provides localized surface measurements and may underrepresent elements with uneven distribution (such as Pb) or lighter elements (such as Sn). Despite these limitations, the overall elemental profile supports classification as RG7 bronze. In the BP, sulfur accounts for 14.5 %, making it the primary element after copper. In contrast, GP contains significant levels of oxygen (25.5 %), and chloride (4.2 %).

Table 2. Elemental EDS analysis of BB, BP and GP samples.

Wt, %	**Cu**	**Sn**	**Zn**	**Pb**	**K**	**C**	**O**	**S**	**Cl**	**N**	**Co**	**Ni**	**Mn**	**P**
BB	82.9	5.2	4.9	2.2	-	3.1	1.6	-	-	-	-	-	0.1	0.1
BP	78.8	0.7	0.7	-	0.3	3.4	1.6	14.5	-	-	-	-	-	-
GP	61.4	0.3	1.6	-	0.2	3.2	25.5	0.4	4.2	0.4	1.5	0.8	0.4	-

Cross-sections of BP and GP samples were prepared to examine the thickness and stratification of the patina layers. The optical micrograph of BP cross-section is presented in Fig. 4a, where the red line delineates the surface of the BP layer, measured at a thickness of

1.22 µm. Fig. 4b displays the optical micrograph of the GP cross-section, showing two distinct patina layers. It is evident that the GP formed over the BP. The thickness of the BP layer remains consistent at 1.22 µm, while the GP layer exhibits a thickness of 2.14 µm.

Fig. 4c shows SEM images of the cross-sections of both patinas along with EDS elemental mapping distributions for Cu, Sn, Zn, Pb, C, O, S, and Cl. Copper, tin and zinc are present throughout the entire area analyzed. Lead is detected exclusively within the bronze substrate and is absent from the patina layers.

In Fig. 4c, the lower regions of the cross-sectional images represent the bronze substrate underlying the patina layers. The microstructure observed here—comprising a typical α-Cu matrix with discrete, bright Pb-rich inclusions—is consistent with the features previously described for the etched BB sample (Fig. 2a). EDS elemental mapping confirms the presence of Sn and Zn within the matrix, particularly concentrated in the interdendritic regions. As the BP and GP samples were fabricated from the same RG7 bronze batch and subjected to the same polishing procedures as the BB samples, the substrate microstructure in Fig. 4c accurately reflects that of BB. This confirms that the essential microstructural characteristics of the bronze alloy have been reliably captured and visualized.

For BP, a distinct sulfur-rich layer is evident with the application of K_2S during its preparation. Oxygen is observed both within and above the sulfide layer, aligning with regions of high sulfur concentration.

The GP consists of two distinct layers: the first layer is predominantly sulfur-dominated (the black patina), while the second is characterized by a chlorine content. A strong oxygen signal is present throughout the entire green chloride patina layer.

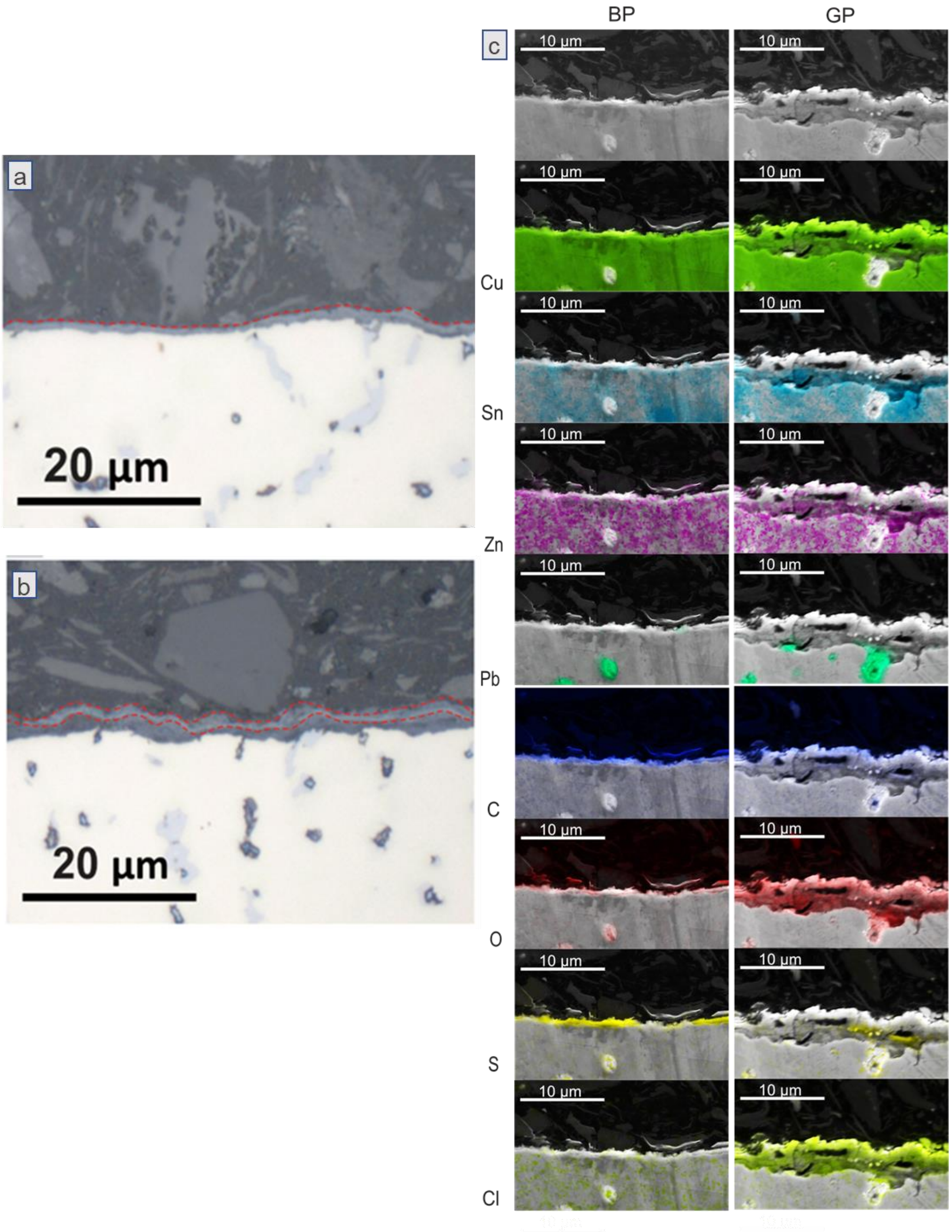

Figure 4. Metallographic cross-sections of (a) BP and (b) GP samples, along with (c) SEM images and EDS elemental mapping of the BP and GP cross-sections.

Raman and FTIR-ATR spectroscopy were employed to determine exact composition of the patinas. The FTIR spectrum of BP did not exhibit well-defined peaks and is therefore not presented. However, the spectrum of BP closely correlated with reference spectra for the mineral romarchite (SnO), with a characteristic peak observed at 515 cm⁻¹.

During the Raman spectroscopy measurements on BP, three distinct regions were observed on the BP samples, related to different thickness of patina. Spectra was recorded from each of these regions, which are labeled as black, red, and green in Fig. 5. The results indicated that all three regions have the same composition with the BP consisting primarily of the mineral anilite (Cu_7S_4). A reference spectrum of anilite obtained from the Raman spectra X-ray diffraction database is also shown in Fig. 5 (blue line). The recorded spectra of the BP exhibited a sharp peak at 474.4 cm^{-1} and a less intensive peak at 266.4 cm^{-1}, both of which align with the reference peaks of anilite. Notably, the IR spectra did not reveal any peaks associated with anilite, consistent with its inactivity in the infrared region [40].

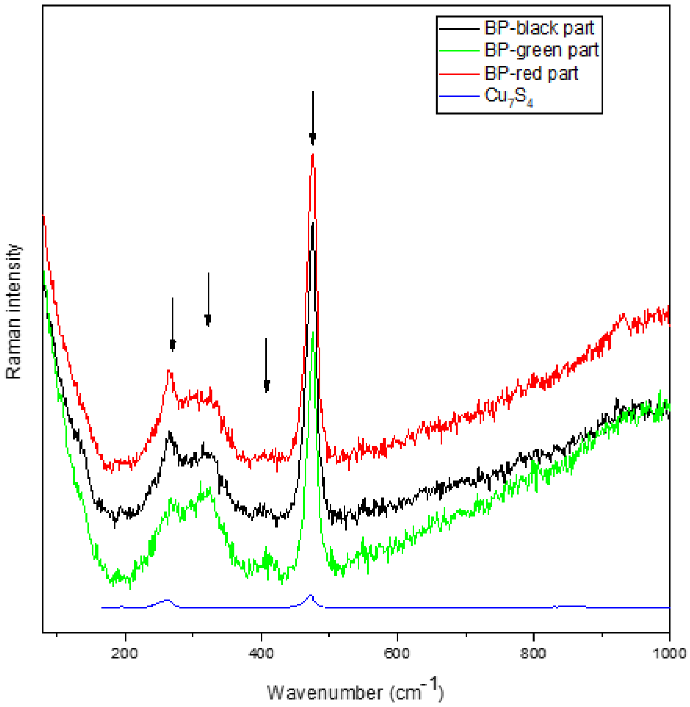

Figure 5. Raman spectra of BP recorded on different locations and anilite reference (Cu_7S_4).

No peaks characteristic of green chloride patina were observed in the Raman spectrum of GP, likely due to the use of a 632 nm excitation laser. Copper hydroxychlorides, such as atacamite and paratacamite, exhibit low Raman activity under 632 nm laser excitation and are more effectively detected using 532 nm excitation [41]. Since the Raman spectrometer used in this study was equipped only with a 632 nm laser, FTIR-ATR was employed as a complementary technique to enable compound identification. Fig. 6 presents the FTIR-ATR spectrum obtained on GP. The bands at 3438 and 3328 cm^{-1} are associated with the stretching of the O-H bond of the hydroxy group, those between 984 and 819 cm^{-1} are associated with the deformation vibration of the same bond, while bands between 602 and 460 cm^{-1} are assigned to the stretching of Cu-Cl and Cu-O bonds, characteristic of the basic copper chlorides ($Cu_2(OH)_3Cl$), such as atacamite and isomorph.

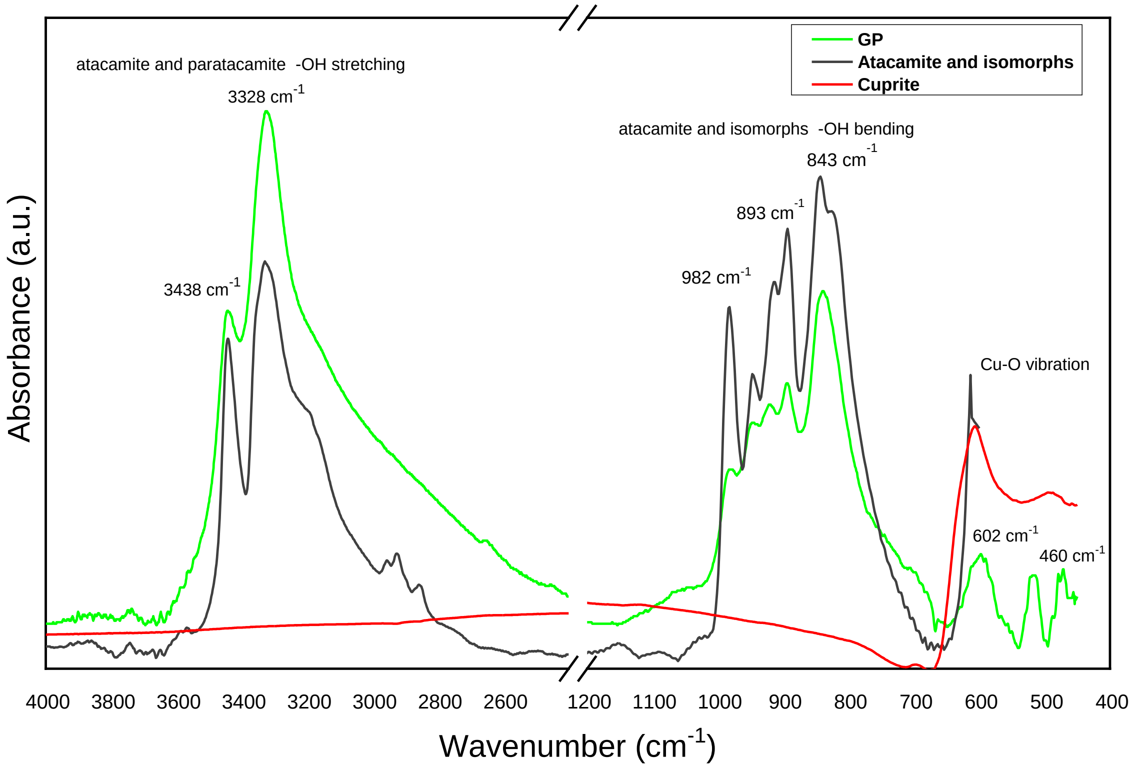

Figure 6. FTIR-ATR spectra of GP, compared to references of cuprite and basic copper chlorides ($Cu_2(OH)_3Cl$), such as atacamite and its isomorphs.

3.2. Protection of patinas by nanocoatings

The three types of samples—BB, BP and GP—were subjected to two coating treatments: (i) the formation of a behenic acid SAM and (ii) a crosslinked layer of behenic acid achieved through ionizing radiation (PNC). A schematic representation of these processes is shown in Fig. 7a. To assess the impact of these coatings on the surface properties, the hydrophobicity of the samples was evaluated by measuring the water contact angle. Fig. 7b shows the variations in water contact angle for each type of sample, comparing values before and after the application of the coatings.

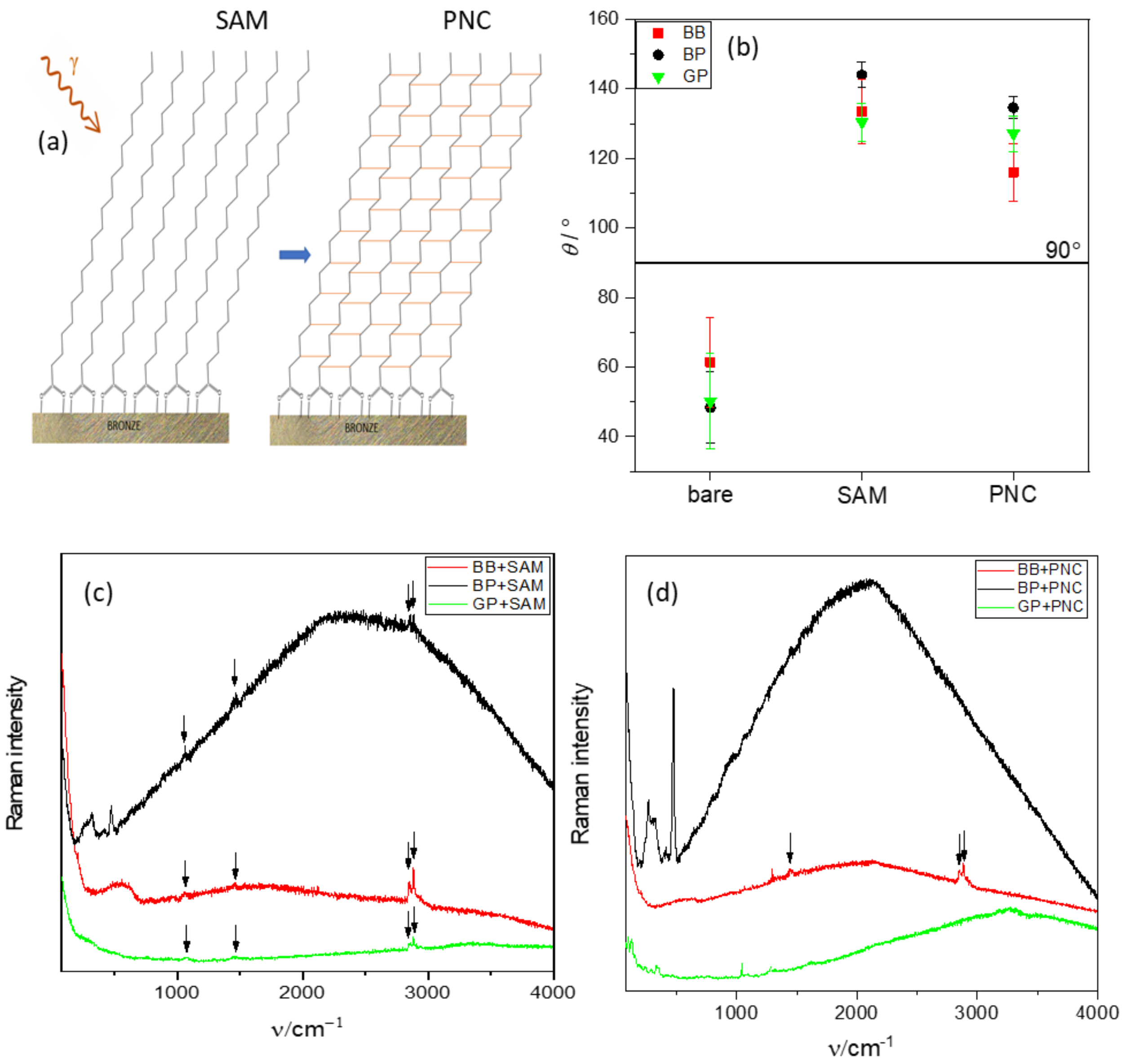

Figure 7. (a) Schematic presentation of crosslinking of SAM of behenic acid on the bronze surface. (b) Water contact angles measured for BB, BP and GP samples in their untreated state and after treatment with SAM and PNC coatings. Raman spectra of samples coated with (c) SAM, and (d) PNC.

BB exhibits a naturally hydrophilic surface, with a contact angle of approximately 50°, a value typical for metallic surfaces. The application of patinas further enhances hydrophilicity, reducing the contact angle by approximately 10°. However, upon the application of behenic acid, all samples exhibit a significant shift toward hydrophobic behavior, with contact angles well over 90°, falling within the range of 130°–150°. Following irradiation, a slight reduction in contact angles is observed across all samples, likely attributed to the degradation of behenic acid molecules that are not part of the well-ordered self-assembled layer and are too spatially distanced to undergo effective crosslinking.

Figs 7c and 7d present the Raman spectra recorded for all samples coated with SAM and PNC, respectively. The Raman spectra for the SAM-coated samples (Fig. 7c) exhibit four characteristic peaks, consistent for all three samples. The bands characteristic for coating applied are denoted by an arrow in Figs 7c and 7d. The first band, at 1064.0 cm^{-1}, corresponds to vibrations related to C–C stretching. The second band, at 1459.7 cm^{-1}, is associated with –CH_2 bending. The two bands, at 2848.7 cm^{-1} and 2887.6 cm^{-1}, correspond to the symmetric and asymmetric stretching of the -CH_2 group, characteristic of the aliphatic fatty acid chain [42]. These spectral features confirm the presence of aliphatic chains of behenic acid on the surface of the samples.

In the Raman spectra of PNC-coated samples (Fig. 7d), the BB sample retains the same spectral features as its SAM-coated counterpart, indicating that behenic acid remains present post-irradiation and suggesting that the coating has not undergone significant degradation. However, the GP sample exhibits the most complex structure, with the emergence of previously undetected peaks (“hidden peaks”). These peaks are exclusively observed in PNC-coated GP samples and may indicate partial degradation of the coating due to irradiation.

While the persistence of key Raman bands supports the presence of the organic layer, distinguishing between non-crosslinked and crosslinked molecules is not possible through Raman spectroscopy alone. Direct spectroscopic confirmation of crosslinking is particularly challenging on patinated substrates due to the monolayer’s ultrathin nature (<3 nm) and the surface complexity. Therefore, evidence of successful crosslinking and coating stability is provided through comparative electrochemical analyses. It is also important to note that the gamma irradiation dose used (110 kGy) is well below levels known to damage metallic substrates or common patina compounds. Both literature data and experimental observations confirm that irradiation at this dose selectively affects only the organic layer, leaving the bronze and patina chemically and structurally unaltered.

3.2.1. Short-term protective properties of coated samples

To evaluate the short-term protective properties of the coatings, freshly prepared BB, BP and GP samples, both untreated (bare) and treated with SAM and PNC, were exposed to the corrosion solution and polarization measurements were conducted to assess the protective efficiency of the coatings, as described in section 2.2. Although this short-term immersion does not simulate atmospheric corrosion conditions, it provides a standardized environment for comparing the initial corrosion protection performance of the different coatings.

Figs 8a, 8b and 8c present the potentiodynamic polarization curves of BB, BP, and GP, both untreated and treated with SAMs and PNCs. The presence of behenic acid on all surfaces leads to a noticeable reduction in corrosion current density (j_{corr}) and a shift toward more positive corrosion potentials, indicating a lower overall corrosion rate. This effect is observed despite minimal changes in the cathodic Tafel slopes in some cases.

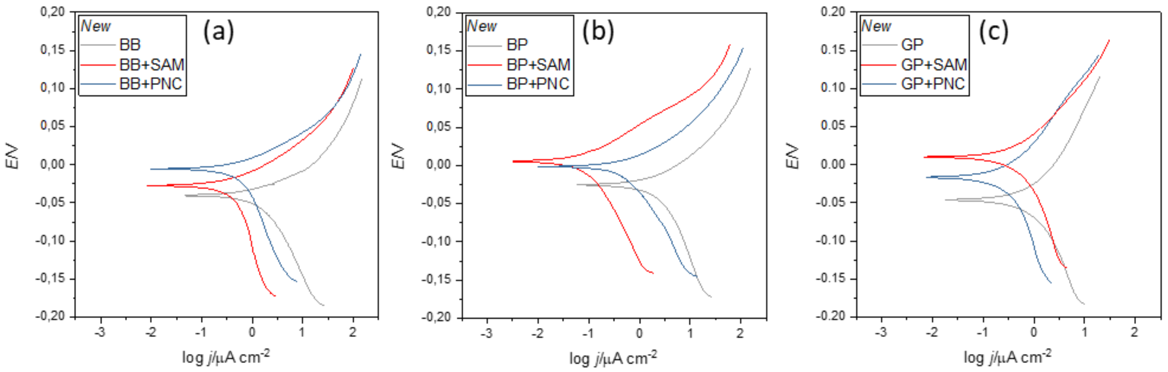

Figure 8. Tafel plots showing the results of polarization measurements on freshly prepared samples of (a) bare bronze (BB), (b) black patina (BP), and (c) green patina (GP), each in untreated (bare), SAM-coated, and PNC-coated states in the corrosion test solution.

In BP and BB samples, both anodic and cathodic branches are altered by the SAM and PNC coatings, indicating strong interactions with the bronze and sulfur-rich patina. For GP, the slope of the cathodic branch and diffusion-limited current, when referenced to overpotential, remain essentially unchanged. In contrast, the anodic branch shifts to lower currents and the corrosion potential is ennobled, together indicating predominant inhibition of anodic dissolution. Consequently, the treatment mainly suppresses the anodic process, with negligible influence on the cathodic kinetics. This specific behavior in GP can be attributed to differences in the presence and stability of loosely adsorbed behenic acid molecules. In SAM-coated samples, especially on rough and porous patinas like GP, a substantial fraction of the behenic acid does not form a compact, ordered monolayer but remains loosely bound. These disordered molecules, while not stable, temporarily enhance surface coverage and reduce j_{corr}, particularly by modulating interfacial charge transfer and suppressing corrosion reactions at the corrosion potential.

However, these loosely adsorbed molecules are not durable, and their contribution to corrosion protection is not expected to persist under environmental exposure. Upon gamma irradiation, these molecules are selectively degraded, leaving behind a more compact and stable crosslinked film, but only where the monolayers were successfully formed. As a result, in GP samples, the PNC coating achieves substantially lower j_{corr} values than the SAM.

This observation highlights the nuanced relationship between coating structure and substrate type: while SAMs may outperform PNCs initially on smoother or less reactive surfaces (BB, BP), their performance may degrade under environmental stress, especially due to the instability of the loosely adsorbed fraction.

The corrosion current densities (j_{corr}), determined by Tafel extrapolation (Figure 9a), support these observations. It should be noted that while Fig. 8 shows representative curves obtained on specific types of samples, Fig. 9 presents the averaged values of all five same samples that were used for the studies, and it also shows the deviations, thus some differences can be observed.

Across all sample types, the application of behenic acid (whether as a SAM or a crosslinked PNC) leads to a reduction in j_{corr}. The most pronounced improvement is seen in BP samples, where j_{corr} decreases from 1.82 µA cm^{-2} (bare) to 0.07 µA cm^{-2} after SAM treatment.

While irradiation (PNC) leads to an increase in j_{corr} for BB and BP samples compared to SAMs, values remain well below those of untreated surfaces. As discussed previously, for GP samples, j_{corr} further decreases after crosslinking, reflecting the stabilizing effect of PNC on more complex patina structures.

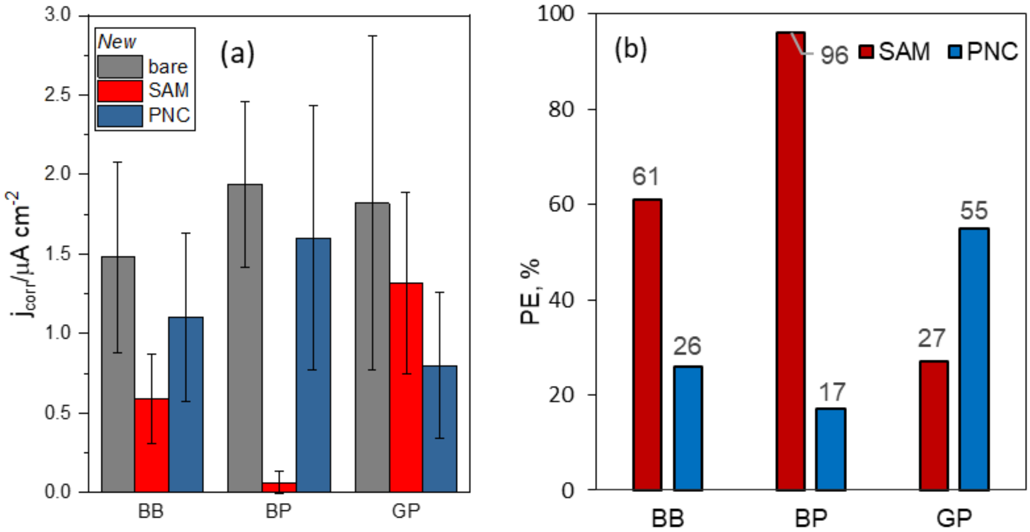

Figure 9. (a) Corrosion current densities (j_{corr}) derived from polarization curves for all samples using the Tafel extrapolation method; (b) protective efficiency of SAM and PNC coatings on BB, BP, and GP samples.

Fig. 9b presents the short-term protective efficiency (PE) of the coatings, calculated using the following equation:

$$PE = \frac{(j^0_{\text{corr}} - j^{\text{s}}_{\text{corr}})}{j^0_{\text{corr}}} \times 100\ \% \qquad (1)$$

where j^0_{corr} represents the corrosion current density of the untreated sample (BB, BP and GP), and j^s_{corr} represents the corrosion current density of the SAM- or PNC treated samples.

From the obtained results, it is evident that the protective efficiency of the SAM coating varies depending on the substrate material. This dependence of protective efficiency on the surface patina type has also been observed for other coating systems, such as wax-based treatments [43], and is confirmed here for behenic acid-based SAMs. As shown in Figure 9b, SAMs exhibit highest efficiency on the sulfur-rich BP (96 %), lower efficiency on BB (61 %), and the lowest on the more complex chloride-based GP (27 %), reflecting the influence of patina composition and morphology on coating performance.

Although PNC underperforms compared to SAM on BB and BP (26 % and 17 % respectively), it provides notably better protection on GP with 55 % PE. These short-term results suggest that SAM coatings may yield high efficiency on certain surfaces, but their performance can vary substantially depending on patina composition and surface morphology. These observations are further examined in the following section through artificial aging of samples.

3.2.2. Behavior of the samples under artificial ageing

To achieve a more comprehensive understanding of the differences between unirradiated and irradiated samples under simulated urban atmospheric conditions, their electrochemical behavior was investigated using electrochemical impedance spectroscopy (EIS).

Two sets of samples were analyzed: freshly prepared samples, which were exposed to the corrosion test solution for one hour (designated as "New"), and artificially UV-Wet-Dry aged samples, as described in paragraph 2.1.4, designated as "Aged". The EIS measurements were performed under the same experimental setup as the potentiodynamic polarization measurements.

Although the aged samples in this study were not characterized using spectroscopic or microscopic techniques such as SEM, FTIR-ATR, or Raman, indirect evidence of coating performance was obtained through visual inspection and EIS analysis. All samples retained their initial appearance after exposure and drying, apart from faint water spots with a slight whitish film, similar to marks that can appear when water evaporates on smooth surfaces. Nonetheless, we focused on corrosion resistance characterization, leaving a more detailed spectroscopic or microscopic analysis of aged samples for future investigation.

Representative impedance spectra recorded for the freshly prepared *new* samples are presented as Nyquist and Bode plots in Figs 10 and 11. The semicircles in the Nyquist plots of new samples (Figs 10a, 10b and 10c) have a larger radius for all samples covered by a SAM, as well as by PNC, compared to unprotected metal samples indicating higher overall impedance and improved resistance to the corrosion process, as well as stability of the samples.

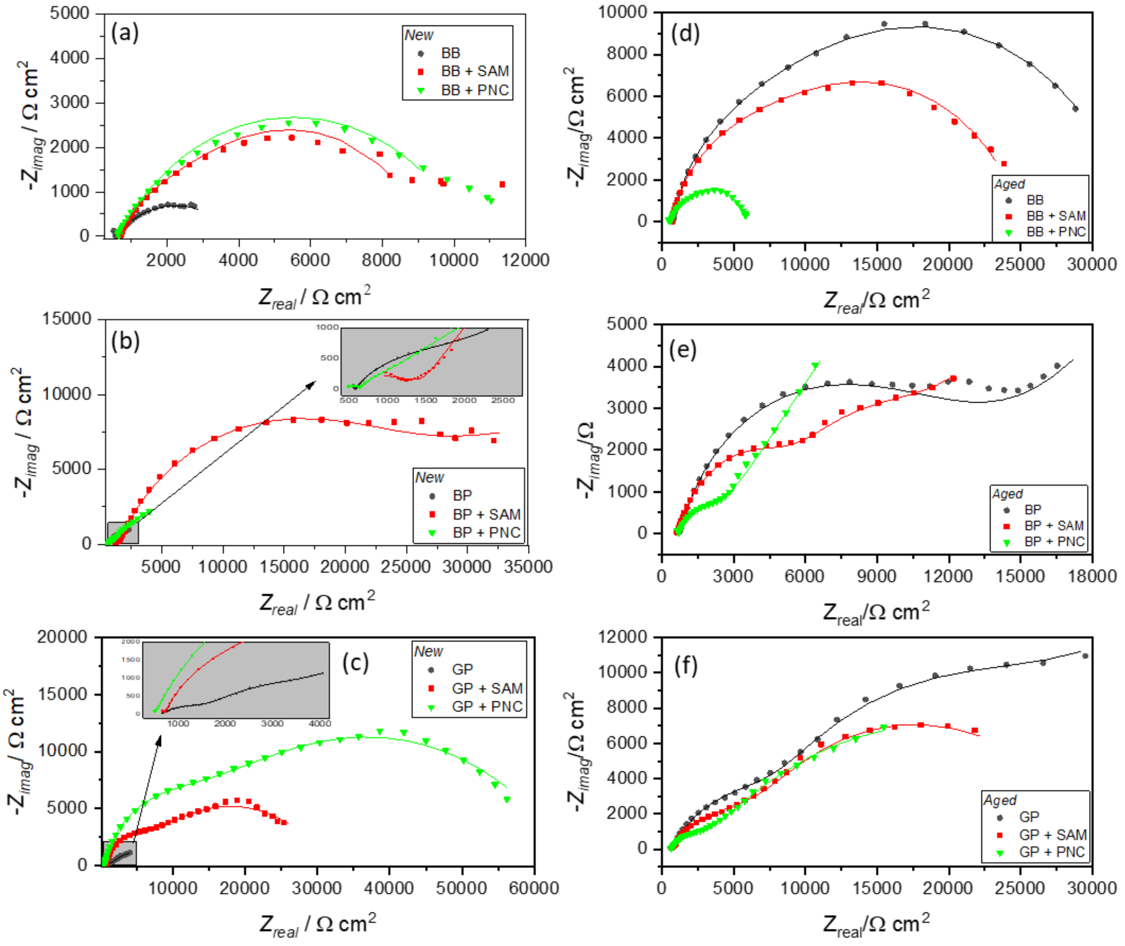

Figure 10. Nyquist plots of electrochemical impedance spectra (EIS) for all studied samples before and after artificial ageing.

The impedance modulus values (Figs 11a, 11b and 11c) show the same behavior, with moderately higher impedance modulus values observed for protected samples. The low-frequency impedance modulus values for protected samples are typically less than one order of magnitude higher than those of unprotected ones. While this indicates a measurable improvement in corrosion resistance, it is relatively modest compared to other coating systems on unaged patinated bronze, in accordance with the very low thickness of the coatings.

The trends are consistent with the observations from the Tafel results. Furthermore, all samples display at least two distinct time constants that can be seen in both Nyquist and Bode plots of all samples, indicating the presence of multiple electrochemical processes contributing to the overall impedance response.

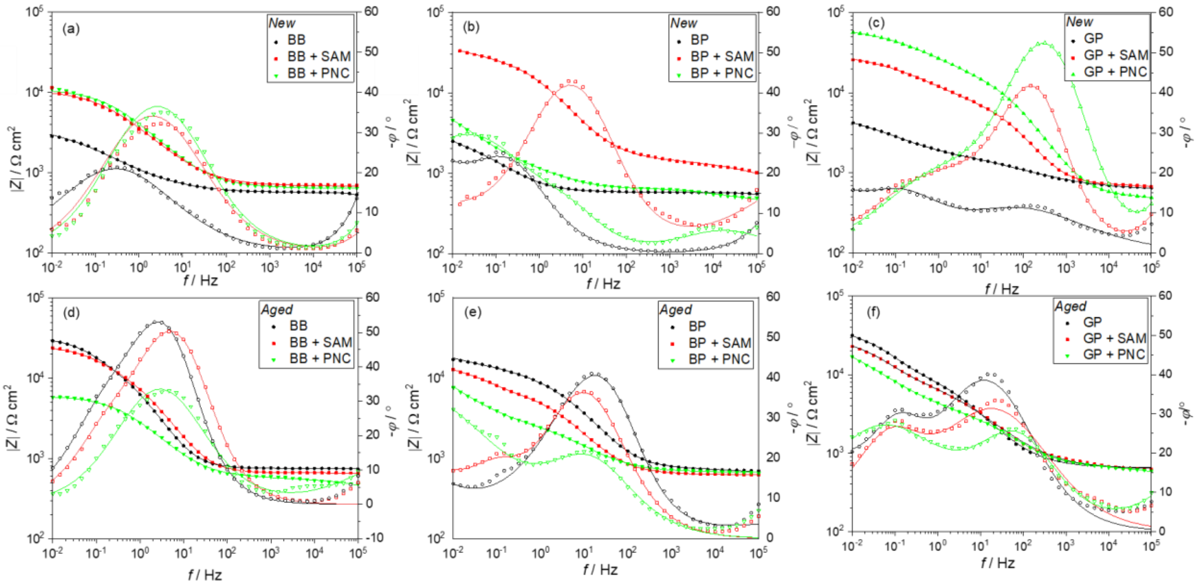

Figure 11. Bode plots of electrochemical impedance spectra (EIS) for all studied samples before and after artificial ageing.

Electrochemical impedance spectra were analyzed by fitting the experimental data to equivalent electrical circuits (EECs), commonly used for patinated metals and organic coatings. The applied models are summarized in Table 3, and representative fits are shown in Figures 10 and 11, where symbols denote the experimental data and solid lines represent the fitted curves. Model selection was based on both statistical quality of fit, evaluated via the lowest chi-squared (χ^2) values and minimal residuals, and physical relevance of the extracted parameters, such as realistic capacitance and resistance values consistent with the sample composition and morphology. The excellent agreement confirms the adequacy of the selected models in describing the system behavior.

Three EECs were used depending on the sample type and behavior: 2RQ, 2RQ-W, and 3RQ. Each circuit includes an electrolyte resistance (R_{el}) between the working and reference electrodes, along with two or three resistance–pseudocapacitance (R–Q) pairs. The 2RQ-W model also includes a Warburg element (W) to account for diffusion-controlled processes, where mass transport limitations are present.

The Warburg impedance models diffusion-controlled processes by decribing the impedance response of semi-infinite linear diffusion to a planar electrode surface. It is characterized by a frequency-dependent behaviour where both real and imaginary components of the impedance vary proportionally to the inverse square root of angular frequency ($\omega^{-1/2}$), representing mass transport limitations. The Warburg coefficient (σ) quantifies the magnitude of the diffusion impedance.

All capacitive elements were modeled as Constant Phase Elements (CPEs) to account for the non-ideal behavior typical of patinated or heterogeneously coated surfaces. The use of CPEs reflects the non-ideal capacitive behavior typically observed at metal/patina interfaces, which can arise from surface heterogeneities, roughness, and compositional variation. Using a pure capacitance in such systems can lead to significant inaccuracies [44,45].

Table 3. The equivalent electrical circuits (EEC) used for fitting the experimental EIS data.

Equivalent circuit (EEC)		**Fitted samples**	
		New	**Aged**
2RQ-W	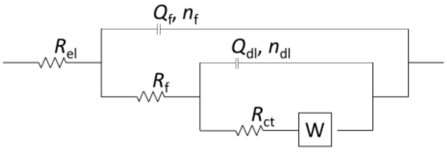	BP, GP	BP, GP BP+SAM, GP+SAM BP+PNC
2*RQ*	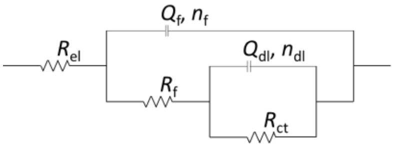	BB BB+SAM BB+PNC	BB BB+SAM BB+PNC
3*RQ*	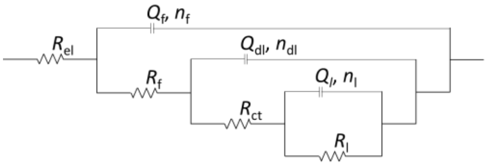	BP+SAM, GP+SAM BP+PNC, GP+PNC	GP+PNC

The first *R*-*Q* pair, present in all EECs, describes the corrosion reaction at the metal-solution interface. In this pair, R_{ct} represents the charge transfer resistance, while Q_{dl} represents the non-ideal double-layer capacitance.

The second *R*-*Q* pair, also present in all EECs, is associated with high-frequency responses and characterizes the properties of a surface film formed on the samples. This film is described by its resistance (R_f) and a pseudocapacitance (Q_f) that reflects the dielectric properties of the layer. Although all samples possess a surface film, its composition varies depending on the sample type. For instance, BB samples exhibit an oxide layer, whereas BP and GP samples consist of a patina layer.

The third *R*-*Q* pair, included in the 3*RQ* model, corresponds to an additional loosely bound outer layer (e.g., disordered organics or unstable patina components) present in certain samples. This element is associated with the ionic and dielectric properties of this superficial material and represents a non-faradaic physical barrier effect rather than a corrosion (faradaic) process. By limiting electrolyte access to the underlying surface, it contributes to the overall impedance. Its disappearance after aging indicates that the layer has been removed or rearranged. This layer is characterized by its resistance (R_l) and a corresponding pseudocapacitance (Q_l).

To enable meaningful interpretation and comparison, the CPE parameters extracted from the fitting were converted into capacitance values using the Brug formula [45]:

$$C = (Y_0 \cdot R^{1-n})^{1/n} \tag{2}$$

where Y_0 is the CPE admittance (in $S \cdot s^n \cdot cm^{-2}$), n is the CPE exponent ($0 < n \leq 1$), R is the resistance associated with the same time constant (e.g., R_{ct} or R_f or R_l). This conversion enables physically meaningful comparisons across different systems by approximating the effective interfacial capacitance despite inherent non-idealities. The CPE exponents (n_{ct}, n_f, n_l) ranged from 0.50 to 1.00, reflecting varying degrees of surface heterogeneity. Values closer to 1 indicate more homogeneous, ideally capacitive behavior, while lower values suggest increased roughness or compositional disorder.

Capacitance values derived from this method are reported in Table 4, and throughout the text, references to "capacitance" refer to these CPE-derived values unless stated otherwise. A clear qualitative correlation can be observed between the EIS parameters and the corrosion current densities obtained from potentiodynamic polarization measurements (Fig. 9a). Samples that demonstrated higher total resistance values ($R_{ct} + R_f + R_l$) consistently exhibited lower j_{corr} values, reflecting improved corrosion resistance. This trend is evident across all coating types and substrates in the unaged condition.

In most samples—both coated and uncoated—we consistently observe that the capacitance of the surface film (C_f) exceeds that of the electrochemical double layer (C_{dl}). This trend aligns with established understanding for systems involving oxide layers, organic coatings, or patinas formed on rough or porous metallic substrates. In such cases, the surface film contributes significantly to the overall dielectric response due to its inherent structure, composition, and increased effective surface area, while concurrently limiting electrolyte access and thus reducing the contribution of C_{dl}.

For uncoated samples (e.g., BB), this behavior can be attributed to the spontaneous formation of a native oxide or hydroxide layer during atmospheric exposure, as well as during the 45-minute open-circuit potential (OCP) stabilization in mildly acidic conditions (pH 5). Additionally, surface roughness from P1000-grade polishing (samples were not mirror-polished) further enhances the dielectric properties associated with C_f. These combined effects result in a pronounced film capacitance even in the absence of an applied coating. Such observations are well-supported in the literature, particularly in studies of rough or coated metal surfaces where C_f dominates the high-frequency impedance response [51] and this behavior remains consistent across nearly all tested conditions.

BB samples

For BB samples, the *2RQ* model commonly used for fitting bronze corrosion systems [48] provided the best fit for the EIS data. For the BB+SAM and BB+PNC datasets, small deviations between the fitted and experimental curves were observed at the lowest frequencies (final two–three points), consistent across all replicates. These deviations indicate the onset of a secondary process that is not fully developed and cannot be reliably modeled by adding another circuit element without over-parameterizing the fit and degrading agreement in the main frequency range. The fits were therefore performed within the stationary frequency window, excluding these terminal points.

The fitting results, presented in Table 4, show that R_{ct} remains relatively constant across all new samples (BB, SAM and PNC). However, the R_f increases upon the application of behenic acid, both for the SAM and PNC coatings, rising from 3×10^3 to 2×10^4 kΩ·cm^2 for SAM, and 4

× 10^3 kΩ·cm^2 for PNC. This trend is consistent with the observations from polarization measurements.

EIS data further reveal that the film resistance is higher for SAM samples, which also exhibit lower effective film capacitance values compared to PNC. This suggests that the SAM layer is more compact and dielectric-efficient [29]. After irradiation, successfully self-assembled behenic acid molecules undergo crosslinking, while poorly organized molecules degrade, leading to a decrease in film resistance [33]. While this process stabilizes the remaining structure, it may also introduce local inhomogeneities or reduce the overall dielectric integrity, resulting in a modest increase in capacitance. The superior short-term protective efficiency of the SAM layer is attributed to its high surface coverage [26], though its inherent structural disorder can compromise long-term stability.

A consistent trend is observed between EIS and polarization data: samples with higher impedance ($R_{ct} + R_f + R_l$) generally exhibit lower corrosion current densities, confirming the protective effect of the coatings.

For the aged BB samples (Table 4), the resistances are significantly higher for the uncoated (bare) samples compared to their freshly prepared counterparts, while simultaneously, the double-layer capacitance (C_{dl}) also increases. This concurrent increase suggests the formation or densification of a surface layer during aging, which may temporarily limit ionic transport.

A slight decrease in C_f, coupled with an increase in R_f, for aged SAM samples indicates that the protective layer has begun to stabilize and effectively cover the surface. For these aged SAM-coated samples, a higher C_{dl} value compared to new samples is also observed, accompanied by an increased R_{ct}, suggesting the formation of corrosion products on the surface.

However, the behavior of the surface film differs from that of the bare samples. Specifically, an increase in C_f and a decrease in R_f suggest that the formation of corrosion products has only recently begun and remains actively progressing. This indicates that while the SAM coating has provided a certain degree of protection to the bronze, its effectiveness is only temporary and diminishes over time.

In contrast, the aged PNC-coated samples exhibit minimal changes compared to the new samples, with the only significant variation being a moderate increase in C_{dl}. This increase suggests that the PNC film likely remains intact and stable on the surface; however, in the absence of direct material characterization after aging, we cannot exclude the contribution of other factors, such as partial degradation or surface contamination.

BP samples

For BP samples, the bare metal exhibits diffusion through the patina layer, as indicated by the presence of the Warburg element in the *2RQ-W* element used for data fitting. The corresponding Warburg coefficient reported in Table 4 ($\sigma \approx 4 \times 10^{-3}$ S·s$^{1/2}$/cm^2) reflects the contribution of diffusion impedance through the patina, suggesting that the patina layer permits ionic transport over time [52]. In contrast, SAM- and PNC-coated BP samples did not require inclusion of a Warburg element to achieve satisfactory fits, suggesting that semi-infinite diffusion no longer dominates the impedance response. However, the CPE exponents associated with these coatings remain relatively low ($n \approx 0.5–0.6$), indicating a still-non-ideal, partially diffusive interfacial behavior. This points to a reduction—but not complete elimination—of ionic transport processes, consistent with a transition from long-range diffusion to more localized or finite-length transport within the heterogeneous patina/coating interface, suggesting that freshly coated BP surfaces exhibit markedly reduced diffusion-driven degradation.

Upon the application of the SAM coating, a third time constant could be resolved in the fitted model, represented by an additional R_l-C_l pair with both high resistance and high capacitance values. This feature may reflect the presence of a loosely bound or spatially heterogeneous surface layer rather than a distinct electrochemical interface, consistent with the expected non-uniform organization of behenic acid molecules on the rough patinated surface. Meanwhile, the R_f-C_f pair associated with the patina layer exhibits an increase in R_f and a decrease in C_f. This behavior suggests that as the patina is present on the surface, the surface roughness is greater than for bare bronze, allowing the behenic acid to form a less compact layer on the surface as opposed to bare bronze.

However, the simultaneous presence of a large number of adsorbed behenic acid molecules on the surface, contributing to an additional R_l-C_l pair, leads to an overall increase in surface resistance. The high C_l value of 2×10^{-4} $S \cdot s^n/cm^2$ suggests that this loosely bound layer is not dielectric-efficient and likely structurally unstable. Some of these loosely bound molecules may also contribute to the increased C_{dl} observed for SAM-coated samples, compared to unprotected BP, indicating increased surface heterogeneity or porosity.

The freshly prepared PNC samples display different electrochemical behavior. Although they also exhibit a loosely bound outer layer (R_l), both R_f and R_l are significantly lower than those of the SAM-coated sample, while C_f and C_l are higher. This suggests partial degradation of a behenic acid molecules present on the surface which are not part of a compact layer.

In the aged samples, the loosely adsorbed behenic acid molecules are no longer present on the surface, as indicated by the absence of the R_l-C_l pair in both SAM- and PNC-coated samples. Additionally, the increase in capacitance values for the SAM-coated samples suggests that the compact film has undergone partial dissolution over time. Notably, while the aged BP sample exhibits a reduced diffusion response compared the new sample (σ decreases from $\approx 4 \times 10^{-3}$ to $\approx 1 \times 10^{-3}$ $S \cdot s^{1/2}/cm^2$), diffusion also persists in the aged SAM- and PNC-coated samples, showing that long-term ionic transport through the patina is not fully prevented once the loosely bound molecules are removed from the surface.

After aging and the removal of loosely adsorbed behenic acid molecules on PNC samples, the C_{dl} values decrease to levels comparable to those of the freshly prepared bare sample, dropping from 6×10^{-6} S·s^n/cm^2 for new-BP-PNC to 3×10^{-9} Ss^n/cm^2 for aged-BP-PNC. Meanwhile, other impedance parameters remain largely unchanged, indicating that the PNC coating effectively stabilizes the BP surface, similar to its protective effect on BB samples.

GP samples

The bare GP sample exhibits similar electrochemical properties to the BP sample, except for a significantly higher C_{dl} value. Specifically, C_{dl} is on the order of 10^{-9} Ss^n/cm^2 for freshly prepared BB and BP, whereas for GP, it is on the order of 10^{-5} Ss^n/cm^2. As we have shown, the GP is thicker than the BP, which should result in a lower capacitance according to the parallel-plate capacitor equation:

$$C = \varepsilon A/d \qquad (3)$$

where ε is the permittivity of the dielectric material, d is its thickness, and A is the area of the capacitor plates. In the case as for GP when the capacitance increased despite of an increase in thickness, we see that we have an increase in the active surface area which is a result of a more porous structure. The measurement confirms that the green layer of patina is significantly more porous then the black patina layer.

Upon the application of the SAM coating, neither R_{ct} or R_f show significant changes. However, C_{dl} decreases to 10^{-9} Ss^n/cm^2, suggesting that the coating modifies the electrochemical interface and reduces charge transfer effects. Additionally, a loosely bound film, formed by behenic acid molecules, is observed through the R_l-C_l pair, similar to the case of BP. The properties of this layer closely resemble those found in BP samples, indicating a similar interaction between the behenic acid and the surface. In the case of new GP samples, the SAM- and PNC-coated samples show no significant difference in behaviour, protective properties or stability.

After aging, the SAM film is completely removed from the surface, and the sample exhibits electrochemical properties comparable to those of untreated GP. That is evidenced by the absence of the R_l-C_l pair and the similarity in R_{ct}, R_f, C_{dl}, and C_f values to those observed for aged bare GP samples. These results indicate that the SAM layer does not provide long-term stability. In contrast, aged PNC-coated samples still retain the protective film on the surface, with characteristics closely resembling those of freshly prepared samples. The only notable change is an increase in capacitance values, suggesting a slight increase in surface activity over time. However, the data confirm that the protective film itself remains intact and has not undergone significant degradation.

The diffusion behavior in aged GP samples differs markedly from that observed in BP samples. While aged BP samples exhibit diffusion across all surface treatments (bare, SAM, and PNC), aged GP samples show a more selective diffusion pattern. The aged GP bare sample exhibits increased diffusion compared to the new sample with σ rising by an order of magnitude, from 4×10^{-3} to 5×10^{-2} S·s$^{1/2}$/cm^2), indicating that the porous GP becomes more permeable to ionic transport over time. Unlike bare BP, where diffusion decreases after aging, GP shows a progressive enhancement of diffusion through the patina, as reflected by the higher Warburg coefficient. The aged GP SAM sample retains some diffusion characteristics ($\sigma \approx 2 \times 10^{-3}$ $S \cdot s^{1/2}/cm^2$), consistent with partial loss of the protective layer. However, the aged GP PNC sample maintains its 3RQ equivalent circuit without a Warburg element, demonstrating that the crosslinked coating successfully suppresses long-range ionic diffusion even after aging.

Although detailed spectroscopic or morphological characterization of the patinas after artificial aging was beyond the scope of the present study, indirect observations strongly support the interpretation of the electrochemical results. Visual inspection revealed whitish surface deposits and water stains, particularly on SAM-coated samples, which is consistent with the partial loss or degradation of the organic layer. This is also corroborated by the disappearance of the loosely bound film (R_l–C_l pair) in the EIS spectra of aged samples and the convergence of their electrochemical parameters toward those of the uncoated patinated samples. In contrast, the PNC-coated samples retained stable electrochemical characteristics after aging, indicating that the crosslinked coating remained intact and continued to protect the patina layer. These trends confirm that PNC coatings offer more durable corrosion protection, while complementary spectroscopic investigations of aged samples are being conducted in a separate study. Nevertheless, the electrochemical impedance data provide strong indirect evidence regarding coating stability. The PNC-coated samples exhibited stable impedance parameters after aging, with only minor changes in capacitance, indicating preservation of the crosslinked polymer layer. In contrast, SAM-coated samples showed a loss of the loosely bound film and electrochemical behavior approaching that of untreated surfaces, confirming their limited durability. These trends, supported by visual inspection, reinforce the conclusion that crosslinked PNC coatings offer significantly greater long-term stability under simulated atmospheric conditions. Future studies will include detailed post-aging characterization of coating morphology and chemistry, as well as testing on historical or real archaeological bronze samples to validate the findings in more complex, application-relevant environments.

The results demonstrate that BB, BP, and GP samples all exhibit reactivity under simulated atmospheric conditions, confirming that corrosion processes occur on their surfaces. The presence of a SAM coating provides a certain level of protection by delaying the onset of corrosion. However, a significant and lasting reduction in corrosion is only observed in samples where crosslinking occurs, as seen in the PNC-coated samples, which maintain their electrochemical characteristics indicative of protection even after aging.

While EIS analysis provides valuable insights into coating performance, interpretations based solely on curve fitting have limitations and should ideally be supported by complementary techniques such as microscopy or spectroscopy to confirm coating adhesion and stability. Notably, uncoated aged samples exhibited an overall increase in impedance compared to their unaged counterparts, which may be attributed to patina densification or restructuring during artificial aging, leading to reduced ionic conductivity. Although this may confer temporary barrier properties, its long-term effectiveness in stabilizing and protecting heritage bronze surfaces remains uncertain. Future work on real heritage bronze surfaces, combining electrochemical measurements with spectroscopic and microscopic analyses, will help confirm these interpretations and clarify the origin and durability of the observed impedance changes.

3.3. Relevance to cultural heritage conservation

The maximum impedance modulus values observed at 0.1 Hz in this study are lower in absolute terms than the multi-MΩ·cm² values typically reported for high-performance coatings. However, such benchmarks are not always directly applicable to ultrathin coating systems designed for cultural heritage preservation, as they are not the only requirements. In this field, protective layers must meet stringent and often competing requirements: optical transparency to preserve visual and historical integrity, reversibility and removability to allow future interventions, and compatibility with aged or heterogeneous patinas. These constraints generally preclude the use of thick, fully impermeable barrier coatings common in industrial practice. In addition, real outdoor exposure introduces additional challenges such as rain and mechanical abrasion which impose further challenges on maintaining long-term performance.

The present work was designed as a controlled comparison between two systems based on the same saturated fatty acid with a carboxylic anchoring group: an uncrosslinked SAM and its covalently crosslinked PNC. While absolute $|Z|$ and R_p values are moderate compared with some alternative protective coatings, this outcome is consistent with the ultrathin, minimally invasive nature of the systems studied, anchoring molecule used, and its application conditions. The crosslinked PNC nonetheless exhibited a clear improvement in corrosion resistance and retained electrochemical stability during accelerated ageing, indicating its capacity to slow corrosion without compromising the appearance or reversibility required for conservation.

Literature suggests that further optimization—such as employing alternative anchoring groups (e.g., phosphonic acids), increasing alkyl chain length, or constructing mixed/multilayer assemblies—can raise $|Z|$ and R_p. The dipping method used ensured consistent application for laboratory analysis, but brushing and spraying, previously validated for PNCs [34], are more practical for real-world use on historical artifacts. These strategies, while promising, were beyond the scope of the current work and should be addressed in future studies.

A key innovation in this study is the use of ionizing radiation—specifically gamma irradiation at 110 kGy—to induce covalent crosslinking within the SAMs. This technique initiated radical formation without degrading the organic molecules or disturbing the metal substrate and patina. Gamma rays are well-suited for complex forms due to their deep penetration and uniform energy distribution. However, their use is limited by the need for specialized facilities, making them more appropriate for small or transportable objects such as medals, coins, or fragments, as is already in use for decontaminating artifacts made of materials like wood.

A more promising complementary alternative would be the use of electron beam (e-beam) irradiation. Though their penetration depth is shallower, e-beams are well suited to thin-film coatings like PNCs or for localized treatments. Especially low energy e-beams which are smaller, more accessible, and can operate with high dose rates that enable a much faster crosslinking process compared to gamma irradiation.

While the practical deployment of crosslinked SAMs on cultural artifacts will require further procedural refinement and long-term field studies, this work underscores their potential as minimally invasive, stabilizing treatments for patinated bronze in heritage conservation.

Table 4. Results of fitting the experimental EIS data obtained in the corrosion test solution, with the equivalent electrical circuit shown in Table 3 on untreated and treated BB, BP and GP samples. All capacitive elements were modeled as CPEs in the fitting procedure and further converted into capacitance values using eq. (2).

		***C_{dl}*, $S\cdot s^n/cm^2$**	**n_{dl}**	***R_{ct}*, $\Omega\cdot cm^2$**	***C_f*, $S\cdot s^n/cm^2$**	***n_f***	***R_f*, $\Omega\cdot cm^2$**	***C_l*, Ss^n/cm^2**	***n_l***	***R_l*, $\Omega\cdot cm^2$**	***W*, $S\cdot s^5/cm^2$**	***Equivalent circuit***
New samples												
BB	bare	$1.2\pm0.7\cdot10^{-9}$	1.00±0.00	$4.1\pm1.1\cdot10^{2}$	$7.2\pm1.9\cdot10^{-4}$	0.52±0.03	$3.4\pm0.1\cdot10^{3}$	-	-	-	-	*2RQ*
	SAM	$2.5\pm2.3\cdot10^{-9}$	0.82±0.07	$4.4\pm2.0\cdot10^{2}$	$5.4\pm3.1\cdot10^{-5}$	0.69±0.11	$2.4\pm0.3\cdot10^{4}$	-	-	-	-	*2RQ*
	PNC	$4.3\pm0.6\cdot10^{-10}$	1.00±0.00	$5.6\pm 0.5\cdot10^{2}$	$7.2\pm2.7\cdot10^{-5}$	0.66±0.05	$3.9\pm0.4\cdot10^{3}$	-	-	-	-	*2RQ*
BP	bare	$4.2\pm2.9\cdot10^{-9}$	0.84±0.04	$5.8\pm0.4\cdot10^{2}$	$9.0\pm0.1\cdot10^{-4}$	0.69±0.14	$1.2\pm0.5\cdot10^{3}$	-	-	-	$4.0\pm0.4\cdot10^{-3}$	*2RQ-W*
	SAM	$2.7\pm0.2\cdot10^{-6}$	0.50±0.03	$1.4\pm0.3\cdot10^{3}$	$9.6\pm0.3\cdot10^{-6}$	0.68±0.05	$2.2\pm2.6\cdot10^{4}$	$1.5\pm1.2\cdot10^{-4}$	0.56±0.07	$6.0\pm0.8\cdot10^{4}$		*3RQ*
	PNC	$5.7\pm2.8\cdot10^{-6}$	0.51±0.10	$2.4\pm1.3\cdot10^{2}$	$3.5\pm2.7\cdot10^{-4}$	0.69±0.20	$2.3\pm3.6\cdot10^{3}$	$1.1\pm1.2\cdot10^{-4}$	0.74±0.25	$1.3\pm1.1\cdot10^{4}$		*3RQ*
GP	Bare	$6.1\pm5.1\cdot10^{-5}$	0.52±0.17	$9.3\pm0.3\cdot10^{2}$	$4.6\pm1.4\cdot10^{-4}$	0.54±0.10	$4.3\pm1.3\cdot10^{3}$	-	-	-	$3.5\pm0.6\cdot10^{-3}$	*2RQ-W*
	SAM	$2.5\pm2.0\cdot10^{-9}$	0.89±0.07	$6.2\pm1.0\cdot10^{2}$	$1.6\pm0.9\cdot10^{-6}$	0.80±0.08	$1.6\pm2.2\cdot10^{3}$	$1.5\pm0.9\cdot10^{-4}$	0.50±0.05	$1.7\pm0.9\cdot10^{4}$	-	*3RQ*
	PNC	$5.3\pm4.3\cdot10^{-9}$	0.82±0.06	$7.4\pm1.2\cdot10^{2}$	$7.8\pm6.3\cdot10^{-6}$	0.74±0.04	$5.3\pm6.6\cdot10^{3}$	$1.9\pm1.5\cdot10^{-4}$	0.50±0.06	$2.6\pm2.3\cdot10^{4}$	-	*3RQ*
Aged samples												
BB	bare	$2.7\pm0.8\cdot10^{-6}$	0.86±0.00	$1.2\pm0.6\cdot10^{4}$	$8.2\pm2.7\cdot10^{-5}$	0.67±0.00	$2.1\pm0.7\cdot10^{4}$	-	-	-	-	*2RQ*
	SAM	$3.7\pm1.3\cdot10^{-6}$	0.80±0.03	$5.4\pm0.4\cdot10^{4}$	$1.5\pm0.6\cdot10^{-4}$	0.71±0.03	$8.4\pm4.8\cdot10^{2}$	-	-	-	-	*2RQ*
	PNC	$4.6\pm0.8\cdot10^{-7}$	0.63±0.11	$5.3\pm0.1\cdot10^{2}$	$1.1\pm0.2\cdot10^{-4}$	0.64±0.02	$4.9\pm0.8\cdot10^{3}$	-	-	-	-	*2RQ*
BP	bare	$4.9\pm2.9\cdot10^{-5}$	0.50±0.23	$9.3\pm7.1\cdot10^{2}$	$2.4\pm2.3\cdot10^{-5}$	0.61±0.23	$9.1\pm0.1\cdot10^{3}$	-	-	-	$0.8\pm0.1\cdot10^{-3}$	*2RQ-W*
	SAM	$7.2\pm4.2\cdot10^{-5}$	0.68±0.06	$3.9\pm1.7\cdot10^{3}$	$4.7\pm1.8\cdot10^{-4}$	0.79±0.08	$3.5\pm7.4\cdot10^{3}$	-	-	-	$1.3\pm1.0\cdot10^{-3}$	*2RQ-W*
	PNC	$3.4\pm5.3\cdot10^{-9}$	0.92±0.08	$6.4\pm1.4\cdot10^{2}$	$5.9\pm1.7\cdot10^{-5}$	0.67±0.05	$1.2\pm0.8\cdot10^{3}$	-	-	-	$1.7\pm2.2\cdot10^{-3}$	*2RQ-W*
GP	bare	$3.1\pm1.3\cdot10^{-5}$	0.61±0.06	$1.2\pm 0.4\cdot10^{4}$	$1.4\pm0.6\cdot10^{-4}$	0.92±0.11	$1.3\pm0.7\cdot10^{5}$	-	-	-	$5.1\pm1.1\cdot10^{-2}$	*2RQ-W*
	SAM	$2.2\pm1.4\cdot10^{-5}$	0.55±0.07	$1.4\pm 0.7\cdot10^{4}$	$1.2\pm0.5\cdot10^{-4}$	0.80±0.07	$1.7\pm0.7\cdot10^{4}$	-	-	-	$1.8\pm1.6\cdot10^{-3}$	*2RQ-W*
	PNC	$3.7\pm1.1\cdot10^{-7}$	0.51±0.03	$6.3\pm 0.8\cdot10^{2}$	$5.4\pm1.4\cdot10^{-5}$	0.65±0.00	$1.6\pm0.9\cdot10^{3}$	$1.0\pm1.2\cdot10^{-3}$	0.61±0.14	$1.8\pm2.1\cdot10^{4}$	-	*3RQ*

4. Conclusion

In summary, this study investigated the corrosion behavior of bare bronze (BB) and patinated surfaces (BP and GP) under UV-Wet-Dry artificial ageing and evaluated the protective efficacy of self-assembled monolayers (SAMs) and polymer nanocoatings (PNCs) based on behenic acid. Spectroscopic and microscopic analyses confirmed distinct structural and compositional differences between the patinas, with BP consisting primarily of a sulfur-rich layer and GP forming a dual-layered structure with an outer chloride-rich layer. Raman and FTIR-ATR spectroscopy identified BP as predominantly composed of anilite (Cu_7S_4) and hydrated tin oxide, while GP consisted of basic copper chlorides ($Cu_2(OH)_3Cl$) such as atacamite and isomorphs. These differences influenced surface properties and corrosion susceptibility, impacting the performance of protective coatings.

Electrochemical impedance spectroscopy (EIS) results demonstrated that all surfaces exhibited corrosion activity, with SAM coatings providing only temporary protection due to the progressive removal of loosely adsorbed behenic acid molecules during aging. The presence of an additional time constant in freshly prepared SAM-coated samples indicated a non-uniform, loosely bound film that was removed from the surface over time, resulting in electrochemical properties similar to untreated samples. In contrast, PNC coatings showed superior long-term stability, maintaining their protective function even after aging. Minor increases in capacitance suggested increased surface activity but not film degradation, confirming the durability of the crosslinked polymer matrix.

The results obtained highlight the limitations of SAM coatings in providing sustained corrosion protection, whereas they suggest enhanced adhesion and stability for crosslinked PNC coatings, with a remarkable dependence on surface texture. The approach tested here aims to enhance the stability of reversible organic layers without compromising compatibility with historic patinas or visual appearance. Although dipping was used for uniform film formation, prior studies have shown that SAM application by brushing or spraying is feasible, supporting future implementation on historical bronzes. While the current crosslinking method is not suitable for large-scale conservation use, the promising performance of PNC coatings on patinated surfaces suggests that crosslinked SAM systems warrant further investigation as a platform for developing durable, minimally invasive protection strategies for cultural heritage metals.

Funding

This work was supported by the Croatian Science Foundation [HRZZ IP-2020-02-4344] under the title *Irradiated Polymer Nano-Coatings for Metal Protection (RadMeNano)* and the Scientific-Technological Cooperation with Slovenia under the title *Durability study of bronze protection for outdoor application*, and partially by IAEA Coordinated Research Project (CRP F22082).

References

[1] Petiti C, Toniolo L, Berti L, Goidanich S. Artistic and Laboratory Patinas on Copper and Bronze Surfaces. Applied Sciences 2023;13:11873. https://doi.org/10.3390/app132111873.

[2] Marušić K, Otmačić-Ćurković H, Takenouti H, Mance AD, Stupnišek-Lisac E. Corrosion Protection of Synthetic Bronze Patina. Chem Biochem Eng Q 2007;21:71–6.

[3] Hughes R. The Colouring, Bronzing, and Patination of Metals: A Manual for the Fine Metalworker and Sculptor : Cast Bronze, Cast Brass, Copper and Copper-plate, Gilding Metal, Sheet Yellow Brass, Silver and Silver-plate. 2nd ed. Watson-Guptill Publications; 1991.

[4] Bierwagen G, Shedlosky TJ, Stanek K. Developing and testing a new generation of protective coatings for outdoor bronze sculpture. Prog Org Coat 2003;48:289–96. https://doi.org/10.1016/j.porgcoat.2003.07.004.

[5] Molina MT, Cano E, Ramírez-Barat B. Protective coatings for metallic heritage conservation: A review. J Cult Herit 2023;62:99–113. https://doi.org/10.1016/j.culher.2023.05.019.

[6] Letardi P. Testing New Coatings for Outdoor Bronze Monuments: A Methodological Overview. Coatings 2021;11:131. https://doi.org/10.3390/coatings11020131.

[7] Bostan R, Varvara S, Găină L, Petrisor T, Mureşan LM. Protective effect of inhibitor-containing nitrocellulose lacquer on artificially patinated bronze. Prog Org Coat 2017;111:416–27. https://doi.org/10.1016/j.porgcoat.2016.08.004.

[8] Marušić K, Ćurković HO, Takenouti H. Corrosion Inhibition of Bronze and Its Patina Exposed to Acid Rain. J Electrochem Soc 2013;160:C356–63. https://doi.org/10.1149/2.063308jes.

[9] Otmacic Curkovic H, Kosec T, Marušić K, Legat A. An electrochemical impedance study of the corrosion protection of artificially formed patinas on recent bronze. Electrochim Acta 2012;83:28–39. https://doi.org/10.1016/j.electacta.2012.07.094.

[10] Kosec T, Ćurković HO, Legat A. Investigation of the corrosion protection of chemically and electrochemically formed patinas on recent bronze. Electrochim Acta 2010;56:722–31. https://doi.org/10.1016/j.electacta.2010.09.093.

[11] Marušić K, Otmačić-Ćurković H, Horvat-Kurbegović Š, Takenouti H, Stupnišek-Lisac E. Comparative studies of chemical and electrochemical preparation of artificial bronze patinas and their protection by corrosion inhibitor. Electrochim Acta 2009;54:7106–13. https://doi.org/10.1016/j.electacta.2009.07.014.

[12] Muresan L, Varvara S, Stupnišek-Lisac E, Otmačić H, Marušić K, Horvat-Kurbegović S, et al. Protection of bronze covered with patina by innoxious organic substances. Electrochim Acta 2007;52:7770–9. https://doi.org/10.1016/j.electacta.2007.02.024.

[13] Stupnisek-Lisac E, Tadic K, Otmacic H, Mance AD, Takenouti H. Corrosion Protection of Bronze Patina by New Non-Toxic Organic Inhibitors. ECS Trans 2007;2:31–42. https://doi.org/10.1149/1.2408926.

[14] Marušić K, Ćurković HO, Takenouti H. Inhibiting effect of 4-methyl-1-p-tolylimidazole to the corrosion of bronze patinated in sulphate medium. Electrochim Acta 2011;56:7491–502.

[15] Kosec T, Legat A, Ropret P. Raman investigation of artificial patinas on recent bronze protected by different azole type inhibitors in an outdoor environment. Journal of Raman Spectroscopy 2014;45:1085–92. https://doi.org/10.1002/jrs.4532.

[16] Marušić K, Otmačić Ćurković H. Self-Assembling Monolayers of Stearic Acid in Protection of Steel. Croatica Chemica Acta 2018;91:427–33.

[17] Masi G, Josse C, Esvan J, Chiavari C, Bernardi E, Martini C, et al. Evaluation of the protectiveness of an organosilane coating on patinated Cu-Si-Mn bronze for contemporary art. Prog Org Coat 2019;127:286–99. https://doi.org/10.1016/j.porgcoat.2018.11.027ï.

[18] Masi G, Balbo A, Esvan J, Monticelli C, Avila J, Robbiola L, et al. X-ray Photoelectron Spectroscopy as a tool to investigate silane-based coatings for the protection of outdoor bronze: The role of alloying elements. Appl Surf Sci 2018;433:468–79. https://doi.org/10.1016/j.apsusc.2017.10.089.

[19] Chiavari C, Balbo A, Bernardi E, Martini C, Bignozzi MC, Abbottoni M, et al. Protective silane treatment for patinated bronze exposed to simulated natural environments. Mater Chem Phys 2013;141:502–11. https://doi.org/10.1016/j.matchemphys.2013.05.050.

[20] Novak Ž, Kosec T. CORROSION AND PROTECTION OF NON-PATINATED, SULPHIDE and CHLORIDE-PATINATED BRONZE. Materiali in Tehnologije 2022;56:697–704. https://doi.org/10.17222/MIT.2022.641.

[21] Masi G, Josse C, Esvan J, Bernardi E, Martini C, Bignozzi MC, et al. Micro-characterisation of innovative organic coatings applied for the protection of outdoor bronze monuments. The Annual Congress of the European Federation of Corrosion, 20th International Corrosion Congress and Process Safety Congress 2017, 2022.

[22] Kosec T, Novak Ž, Fabjan EŠ, Škrlep L, Sever Škapin A, Ropret P. Corrosion protection of brown and green patinated bronze. Prog Org Coat 2021;161. https://doi.org/10.1016/j.porgcoat.2021.106510.

[23] Masi G, Bernardi E, Martini C, Vassura I, Skrlep L, Švara Fabjan E, et al. An innovative multi-component fluoropolymer-based coating on outdoor patinated bronze for Cultural Heritage: Durability and reversibility. J Cult Herit 2020;45:122–34. https://doi.org/10.1016/j.culher.2020.04.015.

[24] Masi G, Aufray M, Balbo A, Bernardi E, Bignozzi MC, Chiavari C, et al. B-IMPACT project: eco-friendly and non-hazardous coatings for the protection of outdoor bronzes. IOP Conf Ser Mater Sci Eng, vol. 949, IOP Publishing Ltd; 2020. https://doi.org/10.1088/1757-899X/949/1/012097.

[25] Kosec T, Škrlep L, Švara Fabjan E, Sever Škapin A, Masi G, Bernardi E, et al. Development of multi-component fluoropolymer based coating on simulated outdoor patina on quaternary bronze. Prog Org Coat 2019;131:27–35. https://doi.org/10.1016/j.porgcoat.2019.01.040.

[26] Novak Ž, Kosec T. Corrosion and protection of non-patinated, sulphide- and chloride-patinated bronze . Materiali in Tehnologije 2022;56. https://doi.org/10.17222/mit.2022.641.

[27] Ulman A. Formation and Structure of Self-Assembled Monolayers. Chem Rev 1996;96:1533–54. https://doi.org/10.1021/cr9502357.

[28] Ulman A. An Introduction to Ultrathin Organic Films. Elsevier; 1991. https://doi.org/10.1016/C2009-0-22306-3.

[29] Marušić K, Pezić E, Matijaković Mlinarić N, Dubček P, Sancho-Parramon J, Kralj D, et al. Green Nanocoatings Prepared by Crosslinking Self-Assembled Fatty Acids on Metals. Small 2023;19:2301104. https://doi.org/10.1002/smll.202301104.

[30] Norrod KL, Rowlen KL. Ozone-Induced Oxidation of Self-Assembled Decanethiol: Contributing Mechanism for “Photooxidation”? J Am Chem Soc 1998;120:2656–7. https://doi.org/10.1021/ja9738642.

[31] Kaufmann CR, Mani G, Marton D, Johnson DM, Agrawal CM. Long-term stability of self-assembled monolayers on 316L stainless steel. Biomedical Materials 2010;5:025008. https://doi.org/10.1088/1748-6041/5/2/025008.

[32] Zhang Y, Terrill RH, Bohn PW. Ultraviolet Photochemistry and ex Situ Ozonolysis of Alkanethiol Self-Assembled Monolayers on Gold. Chemistry of Materials 1999;11:2191–8. https://doi.org/10.1021/cm990140b.

[33] Marušić K, Matijaković N, Mihaljević B. Influence of Gamma Irradiation on a Fatty Acid Self-Assembling Coating of Copper. J Electrochem Soc 2018;165:C973–9. https://doi.org/10.1149/2.1301814jes.

[34] Pezić E, Mlinarić NM, Kovač J, Dubček P, Kralj D, Marušić K. Optimizing the preparation of polymer nanocoatings by self-assembly and gamma irradiation of elaidic acid on copper surfaces. Prog Org Coat 2024;192:108514. https://doi.org/10.1016/j.porgcoat.2024.108514.

[35] Pfeifer ÉK, May Z, Mohai MP, Mink J, Gyurika IG, Telegdi J. Increasing the Resistance of Steel and Austenitic Stainless Steels Against Pitting Corrosion by a γ-Irradiated Self-Assembled Amphiphilic Molecular Layer. Coatings 2024;14:1601. https://doi.org/10.3390/coatings14121601.

[36] Pezic E, Mijic H, Mihaljevic B, Marusic K. The effect of media to reduce irradiation dose in crosslinking of self-assembled molecular layers. Radiation Physics and Chemistry 2023;213:111235. https://doi.org/10.1016/j.radphyschem.2023.111235.

[37] Constantinides I, Gritsch M, Adriaens A, Hutter H, Adams F. Microstructural characterisation of five simulated archaeological copper alloys using light microscopy, scanning electron microscopy, energy dispersive X-ray microanalysis and secondary ion mass spectrometry. Anal Chim Acta 2001;440:189–98. https://doi.org/10.1016/S0003-2670(01)01061-3.

[38] Kosec T, Ćurković HO, Legat A. Investigation of the corrosion protection of chemically and electrochemically formed patinas on recent bronze. Electrochim Acta 2010;56:722–31. https://doi.org/10.1016/j.electacta.2010.09.093.

[39] Timoncini A, Brattich E, Bernardi E, Chiavari C, Tositti L. Safeguarding outdoor cultural heritage materials in an ever-changing troposphere: Challenges and new guidelines for artificial ageing test. J Cult Herit 2023;59:190–201. https://doi.org/10.1016/j.culher.2022.12.003.

[40] Simonescu CCOPLCC. Synthesis and characterization of Cu7S4 (anilite) obtained from copper: thiosulfate system. Journal of Optoelectronics and Advanced Materials 2008;10:2700–2.

[41] Privitera A, Corbascio A, Calcani G, Della Ventura G, Ricci MA, Sodo A. Raman approach to the forensic study of bronze patinas. J Archaeol Sci Rep 2021;39:103115. https://doi.org/10.1016/j.jasrep.2021.103115.

[42] Sharma SK, Nelson DR, Abdrabu R, Khraiwesh B, Jijakli K, Arnoux M, et al. An integrative Raman microscopy-based workflow for rapid in situ analysis of microalgal lipid bodies. Biotechnol Biofuels 2015;8. https://doi.org/10.1186/s13068-015-0349-1.

[43] Otieno-Alego V, Hallam D, Viduka A, Heath G, Creagh D. Electrochemical impedance studies of the corrosion resistance of wax coatings on artificially patinated bronze. In: Mourey W, Robbiola L, editors. Proceedings of the METAL 98: Proceedings of the International Conference on Metals ConservationProceedings of the METAL 98: Proceedings of the International Conference on Metals Conservation, Draguignan-Figanières: James and James; 1998, p. 315–9.

[44] Gateman SM, Gharbi O, Gomes de Melo H, Ngo K, Turmine M, Vivier V. On the use of a constant phase element (CPE) in electrochemistry. Curr Opin Electrochem 2022;36:101133. https://doi.org/10.1016/j.coelec.2022.101133.

[45] Brug GJ, van den Eeden ALG, Sluyters-Rehbach M, Sluyters JH. The analysis of electrode impedances complicated by the presence of a constant phase element. J Electroanal Chem Interfacial Electrochem 1984;176:275–95. https://doi.org/10.1016/S0022-0728(84)80324-1.

[46] Brug GJ, van den Eeden ALG, Sluyters-Rehbach M, Sluyters JH. The analysis of electrode impedances complicated by the presence of a constant phase element. J Electroanal Chem Interfacial Electrochem 1984;176:275–95. https://doi.org/10.1016/S0022-0728(84)80324-1.

[47] Bostan R, Varvara S, Găină L, Mureşan LM. Evaluation of some phenothiazine derivatives as corrosion inhibitors for bronze in weakly acidic solution. Corros Sci 2012;63:275–86. https://doi.org/10.1016/j.corsci.2012.06.010.

[48] Marušić K, Ćurković HO, Takenouti H. Corrosion inhibition of bronze and its patina exposed to acid rain. J Electrochem Soc 2013;160. https://doi.org/10.1149/2.063308jes.

[49] Marušić K, Otmačić Ćurković H, Supnišek Lisac E, Takenouti H. Two Imidazole Based Corrosion Inhibitors for Protection of Bronze from Urban Atmospheres. Croatica Chemica Acta 2018;91. https://doi.org/10.5562/cca3440.

[50] Marušić K, Otmačić-Ćurković H, Takenouti H, Mance AD, Stupnišek-Lisac E. Corrosion protection of synthetic bronze patina. Chem Biochem Eng Q 2007;21.

[51] Torabi S, Cherry M, Duijnstee EA, Le Corre VM, Qiu L, Hummelen JC, et al. Rough Electrode Creates Excess Capacitance in Thin-Film Capacitors. ACS Appl Mater Interfaces 2017;9:27290–7. https://doi.org/10.1021/acsami.7b06451.

[52] Rahmouni K, Keddam M, Srhiri A, Takenouti H. Corrosion of copper in 3% NaCl solution polluted by sulphide ions. Corros Sci 2005;47:3249–66. https://doi.org/10.1016/j.corsci.2005.06.017.